Holocene deglaciation and glacier readvances on the Fildes Peninsula and King George Island (Isla 25 de Mayo), South Shetland Islands, NW Antarctic Peninsula

Pablo Heredia Barión[1,2,3], Stephen J. Roberts[4*], Cornelia Spiegel[2], Steven A. Binnie[5], Lukas Wacker[6], Joanna Davies[7], Imogen Gabriel[8], Vivienne J. Jones[7], Simon Blockley[8], Emma J. Pearson[9], Louise Foster[4,9], Sarah J. Davies[10], Thomas P. Roland[11], Emma P. Hocking[12], Michael J. Bentley[13], Dominic A. Hodgson[4,13], Chris L. Hayward[14], Robert D. McCulloch[14,15], Jorge A. Strelin[3, 16], Gerhard Kuhn[1]

[1]Alfred-Wegener-Institut Helmholtz-Zentrum für Polar- und Meeresforschung, Geosciences Division, Am Alten Hafen 26, 27568 Bremerhaven, Germany.
[2]University of Bremen, Department of Geosciences, Klagenfurterstr. 2–4, 28359 Bremen, Germany.
[3]Centro de Investigaciones en Ciencias de la Tierra (CONICET-UNC), Vélez Sársfield 1611, X5016GCA, Córdoba, Argentina.
[4]British Antarctic Survey (BAS), Natural Environmental Research Council (NERC), High Cross, Madingley Road, Cambridge CB3 0ET, UK.
[5]Institute for Geology und Mineralogy, University of Cologne, Zuelpicher Str. 49b, Cologne D-50674, Germany.
[6]ETH Zürich, Laboratory of Ion Beam Physics, Schafmattstrasse 20, CH-8093 Zürich, Switzerland.
[7]ECRC Dept. of Geography, University College London, North West Wing, Gower St, London WC1E 6BT, UK.
[8]Dept. of Geography, Royal Holloway, University of London, Egham, Surrey, TW20 OEX, UK.
[9]School of Geography, Politics and Sociology, Newcastle University, Newcastle-upon-Tyne, NE1 7RU, UK.
[10]Aberystwyth University, Department of Geography and Earth Sciences, Aberystwyth, SY23 3DB, UK.
[11]Department of Geography, University of Exeter, Exeter EX4 4RJ, UK.
[12]Department of Geography, Northumbria University, Ellison Building, Newcastle-upon-Tyne NE1 8ST, UK.
[13]Department of Geography, Durham University, Durham DH1 3LE, UK.
[14]School of Geosciences, Grant Institute, University of Edinburgh, The King's Buildings, Edinburgh EH9 3FE.
[15]Centro de Investigación en Ecosistemas de la Patagonia, Coyhaique, Aysén, Chile.
[16]Instituto Antártico Argentino, Convenio MREC - Universidad Nacional de Córdoba, Vélez Sársfield 1611, X5016GCA, Córdoba, Argentina.

*Corresponding author: Stephen J. Roberts (sjro@bas.ac.uk)

This is a pre-print version of a revised manuscript published in The Holocene. The final version is available via the peer-reviewed publication doi link on EarthArXiv. We welcome all comments and feedback, posted on EarthArXiv or sent directly to the corresponding author, Stephen Roberts (sjro@bas.ac.uk).

Abstract

To provide insights into glacier-climate dynamics of the South Shetland Islands (SSI), NW Antarctic Peninsula, we present a new deglaciation and readvance model for the Bellingshausen Ice Cap (BIC) on Fildes Peninsula and for King George Island/Isla 25 de Mayo (KGI) ~62°S. Deglaciation on KGI began after c. 15 cal. ka BP and had progressed to within present-day limits on the Fildes Peninsula, its largest ice-free peninsula, by c. 6.6–5.3 cal. ka BP. Probability density phase analysis of chronological data constraining Holocene glacier advances on KGI revealed up to eight 95% probability 'gaps' during which readvances could have occurred. These are grouped into four stages – Stage 1: a readvance and marine transgression, well-constrained by field data, between c. 7.4–6.6 cal. ka BP; Stage 2: four probability 'gaps', less well-constrained by field data, between c. 5.3–2.2 cal. ka BP; Stage 3: a well-constrained but restricted 'readvance' between c. 1.7–1.5 cal. ka BP; Stage 4: two further minor 'readvances', one less well-constrained by field data between c. 1.3–0.7 cal. ka BP (68% probability), and a 'final' well-constrained 'readvance' after <0.7 cal. ka BP. The Stage 1 readvance occurred as colder and more negative Southern Annular Mode (SAM)-like conditions developed, and marginally stronger/poleward shifted westerly winds led to more storms and precipitation on the SSI. Readvances after c. 5.3 cal. ka BP were possibly more frequent, driven by reducing spring/summer insolation at 62°S and negative SAM-like conditions, but weaker (equatorward shifted) westerlies over the SSI led to reduced storminess, restricting readvances within or close to present day limits. Late Holocene readvances were anti-phased with subaquatic freshwater moss layers in lake records unaffected by glaciofluvial inputs. Retreat from 'Neoglacial' glacier limits and the recolonisation of lakes by subaquatic freshwater moss after 1950 CE is associated with recent warming/more positive SAM-like conditions.

Keywords

Southern Hemisphere westerly winds, palaeoenvironmental change, chronology, geomorphology, diatoms, tephra

Introduction

Field-based reconstructions of Antarctic ice sheet and ice cap deglaciation after the Last Glacial Maximum (c. 26–19 ka) and into the Holocene are important components of ice sheet models used to examine the impact of future ice-melt on rates of regional-global sea-level change (Sugden and Clapperton, 1977; Ó Cofaigh et al., 2014; Lindow et al., 2014; Simms et al., 2018, 2019; Kaplan et al., 2020; Nývlt et al., 2020; Oliva et al., 2020). Despite numerous studies, the Early to Mid-Holocene deglaciation and the number, timing, and extent of Mid- to Late Holocene glacier readvances on the northern Antarctic Peninsula (NAP) and South Shetland Islands (SSI) remains debated (Hall, 2007, 2009; Simms et al., 2011; Watcham et al., 2011; Simms et al., 2011, 2012; Ó Cofaigh et al., 2014; Emslie et al., 2019; Oliva et al., 2019).

Ice-marginal and ice-free coastal areas on the NAP and SSI contain an abundance of readily accessible morphostratigraphic features (e.g., raised beaches), lake sediment records, and glacially transported erratics which can be used to constrain past glacier dynamics (Davies et al., 2013). The glacial history of the Fildes Peninsula in the south-west of King George Island (KGI)/Isla 25 de Mayo, the largest of the South Shetland Islands (Figure 1), has been determined by cosmogenic isotope exposure dating of bedrock, radiocarbon and optically stimulated luminescence (OSL) dating of organic remains embedded in raised beaches and moraines of the ~1250 km^2 Bellingshausen Ice Cap (BIC; also known as the Collins Ice Cap), as well as radiocarbon ages from lake sediments and terrestrial stratigraphic sequences overlying coarse grained sediments and diamictons (Figure 1) (Sugden and John, 1973; Pallàs et al., 1997; Bentley et al., 2005; Seong et al., 2008; Hall, 2010; Watcham et al., 2011; Simms et al., 2012; 2021).

[insert Figure 1.]

Isolation basins, raised beaches, and marine abrasion terraces used to constrain glacio-isostatic adjustment (GIA) (uplift) and changes in relative sea level (RSL) are often regarded as the most reliable archives for establishing deglacial unloading and reloading associated with glacier readvance(s) (Bentley et al., 2005; Johnson et al., 2022). The SSI have a complex geological structure due to their position above a former subduction zone and adjacent to an extending basin in Bransfield Strait (Christeson et al., 2003) and variations in elastic strength and underlying viscosity have not yet been captured in GIA models (van der Wal et al., 2015). Consequently, RSL data from the SSI are more complex than other locations across Antarctica,

and several different RSL curves have been suggested (Pallàs et al., 1997; Bentley et al., 2005; Hall, 2010; Roberts et al., 2011; Watcham et al., 2011; Simms et al., 2012; 2021; Johnson et al., 2022).

While some GIA models (e.g. Whitehouse et al., 2012a) infer changes in ice loading that are consistent with RSL reconstructions based on well-dated isolation basin records from the Fildes Peninsula (Watcham et al., 2011; Roberts et al., 2017), the coarse spatial resolution of GIA models means they are not currently able to reproduce smaller scale isostatic responses and RSL reversals implied by field data (Simms et al., 2012; Whitehouse et al., 2012a; Simms et al., 2018; 2021; Johnson et al., 2022). It is increasingly clear that spatially variable responses of glacio-isostatic uplift are likely to have occurred across the SSI and AP during the Mid- to Late Holocene (Fretwell et al., 2010; Zurbuchen and Simms, 2019), which requires data collection at high temporal resolution across wide areas, and new methods of constraining glacier readvances if we are to better constrain these variations.

In this study, we examined the deglaciation and redavance history of the BIC outlet on the Fildes Peninsula using a combined geomorphologic, stratigraphic, chronological, palaeolimnological and statistical approach to provide new constraints on glacier readvance(s) during the Mid- to Late Holocene. New and published data were used to test the hypothesis that Holocene retreat of the BIC was discontinuous and interrupted by more than one glacial readvance during the Mid- to Late Holocene, rather than a continuous process of glacial retreat.

To achieve this, first, we obtained new minimum Beryllium-10 (^{10}Be) cosmogenic isotope exposure ages for deglaciation from three granitic erratics on the NW marine platform of the Fildes Peninsula and the BIC foreland (Figure 1). Second, we obtained new radiocarbon ages from terrestrial and marine macrofossils that were living on the BIC foreland on the Fildes Peninsula before glacier readvances embedded them into moraines; these samples provide maximum ages of glacier advance. Third, we undertook multi-proxy analyses on a new lake sediment core extracted from Kiteschee Lake and compared these results to basal ages and multiproxy data from previously published lake records on the Fildes Peninsula to determine when deglaciation occurred in different sectors (inner, mid, outer; Figure 1) and how Holocene glacier-climate dynamics impacted on lake ecosystems.

With the addition of these new datasets, the amount of chronological data constraining Holocene glacier fluctuations on KGI were large enough to use probability density phase

analysis to identify 'probability gaps' when glacier readvances could have occurred. In this paper, we identify eight occasions in the Mid- to Late Holocene when glacier readvances could have occurred and examine the mechanisms and impact of deglaciation and glacier readvance(s) on the Fildes Peninsula and across KGI.

Regional setting & Study area

Climate setting

The SSI archipelago is a ~230 km long, ~35 km wide active volcanic arc of 11 major islands, with the Fildes Peninsula located at ~62° S, 58–59° W and ~130 km northwest of the Antarctic Peninsula (Figure 1B). The SSI are located south of the Polar Front (50–55°S), where the southern limb of the Southern Hemisphere westerly wind (SHW) belt converges with the polar cell (Figure 1A). Sandwiched between the high pressure subtropic and Antarctic anticyclones, the SSI island chain has a milder and more humid (wetter) maritime climate than the Antarctic continent with up to ~1000 mm of precipitation per year (typically 300-500 mm per year; Michel et al., 2014a), which maintained a stable to slightly negative glacier mass balance on the BIC between 1970–90 CE, with an equilibrium line altitude (ELA) of ~ 150 m a.s.l. (Turner et al., 2002; Bentley et al., 2009; Falk et al., 2018).

The annual mean air temperature on KGI between 1948 and 2011 CE was -2.5 ºC (Kejna et al., 2013). Mean annual, summer and winter air temperatures at the Russian Bellingshausen Station, on the Fildes Peninsula, between 1968–2021 CE were -2.3±3.1°C, 1.1±0.8°C and -5.9±1.7°C, respectively (BAS READER project – Reference Antarctic Data for Environmental Research; Turner et al., 2004). Mean summer air temperatures above zero and snow-free conditions (at sea level) exist for up to four months between December and March (Michel et al., 2014b).

Intense cyclonic activity through the Drake Passage, associated with the SHW to the north, and the low-pressure circumpolar belt to the south (~66°S) means the SSI experience cloud cover for ~80% of the year (King and Turner, 1997; Bañón et al., 2013). Mean annual, summer and winter wind velocities recorded at Bellingshausen (1968–2021 CE) were 26.5±3.5 km h^{-1}, 23.8±2.2 km h^{-1}, 27.3±3.2 km h-1, respectively. Storms and ~100 km h^{-1} winds are common, and wind directions are predominantly SW/W/NW to NE/E/SE (34% W/NW to E/SE) and rarely along the NE-SW axis (BAS READER project; Turner et al., 2004).

A warming trend across the AP and SSI between 1950 and 1999 CE drove increased rates of glacier retreat, ice-shelf collapse (Vaughan et al., 2003; Meredith and King, 2005) and elevated the ELA on the SSI to greater than 200 m above present sea level (henceforth, m a.s.l.) (Falk et al. 2018). Similar to most other stations on the AP and SSI, temperature data from the Bellingshausen Station exhibit decadal scale variability, which has been linked to the El Niño Southern Oscillation (ENSO) (Oliva et al., 2017). Warming initiated approximately five years prior to El Niño in 1982–3 CE and 1997–8 CE was followed by a cooling trend to 2015 CE and a return to a warming trend between 2015-21 CE. Although a shift to a cooling trend was observed across the northern AP (NAP) between 1999–2015 CE, record summer temperatures have since been measured on the northeastern AP and attributed to an enhanced Föhn effect (Turner et al., 2016; Oliva et al., 2017).

Geology and Glaciation

King George Island (KGI), the largest of the South Shetland Islands, has been subdivided into three tectonic regions: the Fildes Block (Fildes Peninsula), Barton Horst (Barton and Weaver Peninsulas) and the Warszawa Block (Potter Peninsula) (Smellie et al., 1984). Covering an area of 38 km^2, the Fildes Peninsula is the largest ice-free area on the South Shetland Islands. It is composed of predominantly andesitic and basaltic lava bedrock, with some interbedded terrestrial sediments, including shales and conglomerates (Smellie et al., 1984). Most of the Bellingshausen Ice Cap (BIC) foreland was glaciated during the Last Glacial Maximum (LGM) and consists of raised marine platforms up to 180 m a.s.l. formed by basic volcanic rocks of Late Cretaceous to Paleogene-age (John and Sugden, 1971; Smellie et al., 1984; Birkenmajer, 1989). The eastern coastline of the Fildes Peninsula is indented with coves, while the western coast is characterized by sheer sea cliffs and stacks (Hall, 2003).

The elevated island interiors of the SSI are characterized by numerous ice caps and permanent snowfields and the coastal fringes are some of the most extensive ice-free and permafrost areas in Antarctica (Braun et al., 2004; Ó Cofaigh et al., 2014; López-Martínez et al., 2012; Michel et al., 2014a) (Figure 1B). Chlorine-36 (^{36}Cl) exposure ages from glacially striated bedrock on nearby Barton Peninsula from above ~50 m a.s.l. show that progressive ice thinning on KGI, SSI started c. 15,000 years ago (Seong et al., 2008).

The Fildes Peninsula contains a variety of glacial geomorphological and periglacial features (López-Martínez et al., 2012; Michel et al., 2014a). López-Martínez et al. (2012) mapped

raised marine platforms and an active glacier in the mid-inner central Davies Heights area (Figure 1D), while Michel et al. (2014a) described many 'Erosive glacial landforms (overdeepened basin, abraded rocks, rock bars)'. The north-western and northern Fildes Peninsula has numerous periglacial features (cryoturbation and gelifluction landforms) and the BIC is bounded by prominent moraines, referred to as the Shetland I moraine (Hall, 2007; López-Martínez et al., 2012; Michel et al., 2014b). A prominent, and largely featureless, marine platform of pre-Holocene age, at ~40-35 m a.s.l. on the north-western Fildes Peninsula, is more than 7 km long and 1 km wide (John and Sugden, 1971) (Figure 1). This feature is flat to gently undulating and seaward sloping, with a limited number of undated granite erratics on its patterned-ground surface (Barsch and Mäusbacher, 1986; Hall, 2003; López-Martínez et al., 2012; Michel et al., 2014a).

Radiocarbon ages obtained from marine-terrestrial transition sediments and raised beaches have been used to reconstruct past changes in local RSL at several sites across the SSI. These indicate that the thickest part of the SSI ice cap was probably centred on the now ice-free area of the Fildes Peninsula during the LGM (Watcham et al., 2011). The SSI ice cap was possibly separated from the AP ice sheet by the Bransfield Marginal Basin during the LGM, but more likely became independent during the Lateglacial–Interglacial transition (c. 15–12 ka) (John and Sugden, 1971; Fretwell et al., 2010; Watcham et al., 2011; Ó Cofaigh et al., 2014).

Basal lacustrine sedimentary sequences in the mid-southern part of the Fildes Peninsula have been dated to c. 10 cal. ka BP (e.g., Jurasee Lake (Mäusbacher et al., 1989)) and were formed in over-deepened glacial basins. Several former marine embayments with basal sediment ages of up to c. 12 cal. ka BP (Watcham et al., 2011) were transformed into freshwater (isolation) basins when the rate of isostatic uplift outpaced the declining rate of sea level rise during the Early Holocene (Watcham et al., 2011). A well-defined Holocene marine high-stand of 18–15 m a.s.l. occurred on the Fildes Peninsula between c. 8 and 7 ka (Mäusbacher et al., 1989; Watcham et al., 2011).

Methods

Cosmogenic nuclide surface exposure dating of erratics

The cosmogenic isotope concentration accumulated in a superficial rock sample is proportional to the length of time exposed to cosmic rays at the Earth's surface (Balco, 2011). The

cosmogenic exposure age produced depends on the production rate (i.e., the concentration of cosmogenic isotopes produced each year per gram of the relevant mineral), which varies spatially and temporally due to variations in atmospheric depth and geomagnetic field effects (Lifton, 2016). Cosmogenic ^{10}Be has the most well-constrained production rate and can be measured at low concentrations (Balco, 2011), but glacially striated and quartz-rich, granitic bedrock and erratics required for ^{10}Be analysis are rare in the basaltic-andesitic volcanic-arc environment of the South Shetland Islands.

Large boulders >50 cm in diameter on the NW BIC glacial foreland were surveyed and classified. These boulders were deposited as glaciers retreated from offshore LGM limits. Differential GPS (dGPS; WGS84 ellipsoid) data for erratic boulders were obtained using a GPS Trimble Pathfinder ProXH. For geodetic reference, we used the landmark DALL 66019M002 (S62°14′16.335″, W58°39′52.364″, ellipsoidal height 39.376 m) at the Argentine Carlini base, ~17 km from the sampled erratics. dGPS precision is better than 10 cm in all axes, but ellipsoid correction errors are larger.

Three large granitic boulders not incorporated into solifluction planes and till sheets of the BIC foreland were considered most suitable for cosmogenic nuclide exposure dating (Table 1). These erratics showed no signs of significant erosion, and their size and shape meant it is very unlikely they had been overturned. Post-depositional movement was minimized by sampling erratics away from slopes or cliffs. Samples of upper few centimetres of sub-horizontally exposed surfaces were taken with a hammer and chisel (Figure 2C) and the angle to the skyline was measured to calculate topographic shielding (Balco et al., 2008). Surface shielding due to snow cover was minimised by sampling from wind-exposed localities (cf. Johnson et al., 2012, 2017, 2020; Glasser et al., 2014; Lindow et al., 2014). Laboratory analysis for ^{10}Be cosmogenic nuclide surface exposure dating followed the procedures of Kohl and Nishiizumi, (1992) and Binnie et al., (2015) (Table 1, Supplementary Materials for details).

Radiocarbon dating of moraines and stratigraphic sections

Moraines adjacent to the BIC were mapped and interpreted from field observations and satellite images (DigitalGlobe, Catalogue ID: 1030010020C0C900; Google Earth, 2006 and 2011). Contour lines are derived from the Antarctic Digital Database with elevation data (±5 m) obtained from the Instituto Antártico Uruguayo (1997). Radiocarbon ages from moraines and stratigraphic sections were obtained by Accelerator Mass Spectrometry (AMS) dating of marine mollusc shells, terrestrial mosses and seaweed layers embedded in sediments and

represent maximum ages for BIC glacier readvance (Table 2). To reduce the risk of contamination with modern material, all samples for radiocarbon dating were taken from fresh and previously cleaned outcrops or sediment cores, packed in zip-lock plastic bags, and stored at 4ºC. Sample preparation prior to radiocarbon dating analysis was undertaken at the Alfred Wegener Institute Helmholtz Centre for Polar and Marine Research and the British Antarctic Survey. Sample measurements and corrections for $^{13}C/^{12}C$ ratio and calculation of Conventional Radiocarbon Ages were undertaken by ETH Zürich and SUERC, Scotland (Table 2, Supplementary Materials for details).

Calibration of radiocarbon ages from marine samples was undertaken in Oxcal v. 4.4 using the Marine20 calibration curve (Bronk Ramsey, 2009; Heaton et al., 2020, 2022), and a new local marine reservoir age offset (ΔR) of 666±76 ^{14}C years for the South Shetland Islands, which represents the weighted mean ΔR of four radiocarbon-dated marine samples collected prior to 1950 CE from the northern Antarctic Peninsula and Signy Island in the CALIB online Marine20 database (http://calib.org/marine/) (Table 2, S3; Heredia Barión et al., (2023)). Terrestrial samples, Kiteschsee Lake samples and previously published data from Yanou Lake (Roberts et al., 2017), were (re)calibrated using the Southern Hemisphere SHCal20 calibration curve (Hogg et al., 2020) in Oxcal v. 4.4 (Bronk Ramsey, 2009). Post-bomb (>1950 CE) ages were corrected according to $^{13}C/^{12}C$ isotopic ratios from measured pMC with the 'present day' pMC value defined as 107.5% (2010 CE) and calibrated using the SHCal13 SH Zone 1-2 Bomb curve in CALIBomb (Reimer and Reimer, 2004; Hua et al., 2013). There were no significant statistical differences (i.e., beyond two-sigma error ranges) between Holocene radiocarbon ages calibrated using the SHCal13/Marine13 (Hogg et al., 2013) and the ShCal20/Marine20 curves (ShCal13 vs 20: n=19, mean difference ± 1σ = -4±8 years; Marine: n=8, mean difference ± 1σ = -45±8 years); hence, comparisons with published data and age models calibrated using the SHCal13 and Marine13 curves remain valid.

New and published chronological and chronostratigraphic data constraining Holocene glacier readvances from the Fildes Peninsula (n=43), Potter Peninsula (n=29), and KGI (n=76) were compiled and a non-parametric phase model (i.e., a probabilistic version of the Oxcal SUM command) was applied to each dataset using the Bchron v. 4.7.6 in R (Haslett and Parnell, 2008; Parnell, 2021). This analysis provides a Gaussian mixture prior distribution density phase age-range estimate, at 0.68 and 0.95 probability level, constraining periods when glacier readvances could have occurred on the Fildes, Potter and Barton Peninsulas on KGI (FP, PP and BP in Figure 3; Table S2). Density phases produced by similar analysis of published SSI-

wide data were less well-defined, likely reflecting local glacier influences and larger errors for some data, and not considered further. The Rcarbon package v. 1.4.2 (Bevan, 2021) was also used for data analysis and plotting. Mapping was undertaken in Arc-GIS and data was analysed and plotted using the Tidyverse suite of packages in R v. 4.1.0/Rstudio v. 1.4.1717, Sigmaplot v. 14.0, C2 (Juggins, 2007), and MATLAB v. R2021a.

Kiteschsee Lake record

Kiteschsee Lake (62° 11'36.55''S, 58° 57'59.93''W) is located at ~15 m a.s.l. in the eastern-central region of the Fildes Peninsula, ~550 m from the east coast and ~2.6 km from the margin of the BIC (Figure 1D, 2B). It is adjacent to the Davies Heights (>100 m a.s.l.), a previously glaciated part of the former raised marine platform in the mid-central area of the Fildes Peninsula, which supplies meltwater directly into the eastern end of the lake (Figure 1D). Marine sediments at the base of a previously studied sedimentary record from Kiteschsee Lake (Mäusbacher et al., 1989) show that much of the low-altitude central area of the Fildes Peninsula remained below sea-level until c. 7–6 ka (Mäusbacher et al., 1989).

Lithology, geochemistry and chronology: We undertook multi-proxy analyses (diatom, grain size, geochemical and sedimentological analysis) on a 77 cm-long sediment record extracted from the flat-bottomed eastern basin depocentre of Kiteschsee Lake (Figure 4, S1–3) and compared data obtained with published lake records from the Fildes Peninsula. High resolution X-ray fluorescence (ITRAX^{TM}) core scanning (XRF-CS) of bulk sediment was performed at Aberystwyth University contiguously at 0.02 cm (200 µm) intervals following procedures in Davies et al. (2015) and Roberts et al. (2022). Gamma (bulk) wet density, magnetic susceptibility (Bartington Instruments MS2E point sensor, 10 second count time; true χvol data), P-wave amplitude and velocity, and resistivity were measured at 5 mm intervals on a Geotek® multi-sensor core logger (MSCL) at Durham University following standard procedures (Gunn and Best, 1998) (Supplementary Materials for details).

A chronology for the Kiteschsee Lake sediment record was based on two subaquatic freshwater moss ages, six bulk sediment AMS radiocarbon ages, and four tephra correlation ages and established using Bayesian age-depth modelling in BACON v. 2.5 in R (Blaauw and Christen, 2011) (Figure 4, Table 2). Volcanic glass-shard counts, and electron probe microanalysis (EPMA) data and tephrostratigraphic correlation with the nearby Yanou Lake record were used to improve the final age-depth model (Blockley et al., 2005; Roberts et al., 2017) (Figure 4, Supplementary Material for details). Reporting of radiocarbon data and age-depth modelling

parameters follows recommendations in Lacourse and Gajewski (2020). Calibrated ages in the text have been rounded to the nearest hundred years to reflect realistic total (internal and external) uncertainties in radiocarbon dating.

Diatom analysis: Since the Early Holocene isolation history of Kiteschsee Lake is well-established (Mäusbacher et al., 1989), and diatom smear-slide screening tests revealed that samples from 77–47 cm depth had very low diatom concentrations, quantitative diatom analysis focussed on reconstructing high-resolution species compositional changes in the uppermost 47 cm (late Holocene) where diatom preservation was sufficient for meaningful environmental interpretation (Figure 4). Quantitative diatom counting and analysis was undertaken at 1–2 cm intervals on sediments between 47 cm and 5 cm depth (3,680 – -63 cal a BP) and related to XRF-CS data using. Species identifications and ecological preferences followed Jones and Juggins (1995), Jones (2000), Watcham et al. (2011), Sterken et al. (2012; 2015) (Figure 4, S9) and are similar to Kopalová et al. (2011), Kopalová and Van de Vijver (2013) and Bulínová et al. (2020).

Principal Component Analysis (PCA) (Figure S10, Supplementary Materials for details). Diatom compositional turnover (β-diversity in Figure 4, 5) was estimated down-core using Detrended Canonical Correspondence Analysis (DCCA) for the most abundant diatoms (>2%). To infer changes in chlorophyll-a shown in Figure 4, we used the diatom-chlorophyll-a training set developed for the Antarctic Peninsula using data from 61 lakes (Jones and Juggins, 1995). Diatom-based transfer functions were applied in C2 (Juggins, 2007) using simple weighted averaging (WA) and weighted partial least squares (WA-PLS) algorithms. The WA-Inverse transfer function was chosen to reconstruct chlorophyll-a as the RMSE, and average bias were low and displayed a strong relationship (R^2) between measured and diatom-inferred chlorophyll-a (Supplementary Materials for details). Constrained cluster analysis (CONISS) with broken stick analysis was applied to square root transformed datasets using R packages Vegan and Rioja to define significant lithofacies units and diatom zones and their boundary positions (Juggins, 2022; Oksanen, 2014).

Results

Cosmogenic nuclide surface exposure dating of erratics

The three erratic granitic boulders on the NW marine platform shown in Figure 3 gave an error-weighted mean ± internal (external) error cosmogenic surface nuclide exposure age of 6,780±220 (590) years (chi-squared, p-value 0.9718), based on the nearby Patagonian production rate (Kp in Table 1) calibration dataset, and 6,580±209 (442) years (chi-squared p-value 0.9715) based on the global calibration dataset (Ww in Table 1) (Borchers et al., 2016, both using the "LSDn" scaling scheme (Table 1). The relatively small standard deviation of the three ages of ±60 years is a favourable indicator of low analytical uncertainties but omits any systematic bias in the age related to, for example, production rate. Henceforth, we base our discussions on the LSDn scaled age estimates (±external errors) and their weighted mean age of 6,580±440 years (Figure 2; Table 1), as this provides a minimum age constraint for ice retreat coupled with a realistic estimate of external uncertainty, taking production rate uncertainty into account. However, the close agreement of the three exposure ages and the overlap between ages produced using the three different production rate calibration datasets shown in Table 1 implies the samples had negligible pre-exposure and that they were exposed simultaneously on the NW foreland during a period of (potentially) rapid Mid-Holocene glacier retreat.

[insert Table 1.]

[insert Figure 2.]

Radiocarbon dating of moraines and stratigraphic sections

Twenty-five new radiocarbon ages were obtained from ten samples in the Artigas Beach–Valle Norte sections of the Shetland I moraine and its associated glaciofluvial and marine sediments (Figure 2, 3A–C; Table 2). Shells embedded in marine sandy to silty sediments reworked into the central Valle Norte sector of the Shetland I moraine (Figure 2B) returned near-infinite radiocarbon ages >40 cal. ka BP, implying significant reworking of older glaciomarine deposits by the BIC (Table 2). In contrast, shells reworked into till in the Artigas Beach southern sector (Figure 2B) have a mean calibrated age range of 6.6–5.4 cal. ka BP (Table 2), with two distinct 0.95 probability density age phases of 6.8–6.5 and 6.3–5.3 cal. ka BP (Figure 3C; Table S2). The oldest of these ages are broadly coeval with cosmogenic exposure ages of the granite erratics (Figure 3C), which represent a minimum retreat age from the northern and central sectors of the inner BIC foreland, while the youngest are consistent with basal (deglaciation) ages from the inner Fildes Peninsula lake sediment records in the Valle Norte–Artigas Beach sectors (Figure 3C, E) (Watcham et al., 2011; Roberts et al., 2017).

Terrestrial moss fragments in glaciofluvial and glacial sediments from the Shetland I moraine dated in this study have mean age ranges of 2.0–1.2 cal. ka BP into two well-defined 95% probability density phases of 2.1–1.7 cal. ka BP and 1.4–1.1 cal. ka BP (n=13) (Figure 2B, 3A, D; Table S2), suggesting emplacement by limited Late Holocene glacier readvances between 1.7–1.4 and/or after 1.1 cal. ka BP (Figure 3A).

Non-parametric 95% probability density phase modelling of all maximum age constraints from terrestrial mosses and shells emplaced in Shetland I moraines from this study (n=25) and that of Hall (2007) (n=43 in total) revealed up to six 'probability gaps' when the readvance of the BIC on the Fildes Peninsula could have occurred (i.e., when no shells or mosses were living): 7.3–6.8 cal. ka BP, 5.3–3.5 cal. ka BP, 3.1–3.0 cal. ka BP, 2.6–2.2 cal. ka BP, 1.7–1.4 cal. ka BP, <0.2 cal. ka BP (Figure 3A–C; Table S3).

Similar analysis of all new and existing chronological constraints for glacier advance on the Fildes Peninsula (Hall, 2007; this study), the Potter Peninsula (Heredia Barión et al., 2023) and the Barton Peninsula (Oliva et al., 2019) (n=80) identified up to eight 95% 'probability gaps' when readvances could have occurred (7.4–6.6 cal. ka BP, 5.3–4.8 cal. ka BP, 4.5–3.9 cal. ka BP, 3.3–3.0 cal. ka BP, 2.6–2.5 cal. ka BP, 1.7–1.5 cal. ka BP, and <0.7 cal. ka BP) and one 68% 'probability gap' (1.3–0.7 cal. ka BP) (Figure 3D, E; Table S3). Subaquatic freshwater moss with post-bomb ^{14}C ages is a common feature at sediment-water interfaces in lakes on Fildes Peninsula lakes (Figure 1) and likely reflects warmer conditions on KGI since the mid-C20th. Late Holocene 'readvance probability gaps' are broadly anti-phased with maximum to minimum calibrated ^{14}C age ranges constraining subaquatic freshwater moss deposition in lake records from Fildes Peninsula (red bars in Figure 3E).

[insert Table 2.]

[insert Figure 3.]

Kiteschsee Lake record

The new Kiteschsee Lake record shown in Figure 4A, B provides a continuous and well-defined Mid- to Late Holocene record of palaeoenvironmental change and volcanic activity. It is largely devoid of soliflucted ash and catchment reworking that disrupts sedimentation in

other lakes on the Fildes Peninsula and KGI, e.g., Yanou Lake (Figure 4C) (Watcham et al., 2011; Roberts et al., 2017).

Lithology, geochemistry and chronology:

Lithofacies units were defined by cluster analysis of XRF-CS data and are summarised as follows: Units 1–3, 77–60 cm (7.5–5.6 cal. ka BP, mean modelled ages) are composed of poorly sorted olive-brown silt with three prominent fine black ash layers in Unit 2. After deposition of the T5 tephra (Unit 4: 60–58 cm; 5.6–5.5 cal. ka BP), there is a distinct change to a light orange-brown silty-clay at the base of Unit 5. A shift to light-grey clay deposition began as early as 1.7 cal. ka BP, the basal age of Unit 6, at 34 cm. After a return to olive-brown silt in Unit 7, (c. 1.2 cal. ka BP), there is a shift to a light grey clayey-mud with silt and sand-rich layers (Unit 8: 20–12 cm depth; 1.2–0.5 cal. ka BP). Unit 9 (12–5 cm; 0.78– -0.005 cal. ka BP) is composed of laminated olive-brown silt, similar to Units 5 and 7. Unit 10 is a thick subaquatic freshwater moss composed entirely of *Drepanocladus l.* sp. of post-bomb age (1950–2011 CE) (Table 2). Lithofacies units and chronological descriptions for Kiteschsee Lake are summarised in Figure 4 and Table 2.

[insert Figure 4.]

Radiocarbon ages from the 77 cm long sediment record from Kiteschsee Lake are in chronological order, except for a calibrated age of 9,900±240 cal. a BP near the base of the fine grey (glaciofluvial/glaciolacustrine) silt and clay deposits of Unit 8 at 21–22 cm depth (Table 2). Bulk sediments at 7–8 cm, 54.5–55 cm, and 64.5–65 cm depth could not be dated due to insufficient carbon. In summary, the Kiteschsee Lake record has a basal age of 7,470 cal. a BP at 77 cm depth (weighted mean modelled age) (7,820–7,110 cal. a BP min.–max. 95% confidence age range). The mean age-depth model 95% confidence age range is 470 years, with a minimum 95% confidence age range of 4 years at 4.5 cm, in the post-bomb era and a maximum 95% confidence age range of 1,230 years at 51.5 cm; 83% of the measured ages overlap with the age-depth model (95% ranges).

Elevated dry mass accumulation rates and increased sand deposition within Unit 6 and the glaciofluvial/glaciolacustrine Unit 8 are indicative of increased erosion and meltwater input from c. 1.7 cal. ka BP onwards (Figure S3, S8). The radiocarbon age of 9,380±30 ^{14}C years from 21–22 cm depth at the base of Unit 8 had a heavily depleted δ^{13}C value of −32.6 ‰, likely

due to reworking of old (possibly marine) carbon. The uppermost sediments, immediately below the living subaquatic freshwater moss, have a measured radiocarbon age of 1,350±30 ^{14}C years (1.2±0.8 cal. ka BP) implying that bulk sediment radiocarbon ages obtained from Unit 9 are either significantly less influenced by old carbon, sedimentation rates declined, or a hiatus exists between Units 9 and 10. K1–8 are radiocarbon ages shown in Table 2; T1a, T3a, T5 and T7 are correlation ages of tephras in the Yanou Lake record (Table S1).

Downcore changes in XRF-CS Ti, K, Ca, and sand content reflect catchment erosion of (volcanic) bedrock and tephra deposition. These and tephra glass-shard counting revealed the position of several prominent visible volcanic ash (tephra) layers (T1-T7 in Figure 4, S1, S2, S3, S4). Incoherence/coherence scatter ratios (inc./coh.) are a proxy for organic content and were also used to define the precise positions of the visible tephra layers in Figure 4, S2, S3. Glass shard-specific electron probe microanalysis of the two most prominent tephra horizons showed that a tephra peak at 33 cm depth (modelled mean age ±95% confidence interval (CI): 1,690 $\frac{+410}{-230}$ cal. a BP) had a broadly bi-modal basaltic-rhyolite glass shard geochemical composition, and the tephra peak at 58 cm depth (modelled mean age ±95%CI: 5,550 $\frac{+150}{-200}$ cal. a BP) consisted solely of rhyolitic glass shards. The latter was found in a ~6 cm thick tephra deposit between 56 and 62 cm depth and was part of a large, explosive multi-stage eruption between 6-5 cal. ka BP (Figure 4B-D, 5C, S1, S5; Roberts et al., 2017). The shard geochemistry of glass shards from both layers aligns with the magma evolution trend of the Deception Island volcano and is characteristic of post-caldera eruptions from Deception Island (cf. Geyer et al., 2019) (Figure S1-S5, S14-S16, Table S5; Supplementary Materials for details).

Diatom analysis: The Kiteschsee Lake diatom record is characterised by short-term changes in diatom communities superimposed upon the steady ecological and environmental evolution of the lake during the Mid- to Late Holocene. Although certain species found respond directly to climatic variables (temperature, precipitation and wind strength), the overall community structure response in Kiteschsee Lake was primarily associated with changes in lake-ice cover and turbidity, reflected in β-diversity DCCA scores (Figure 4A).

Variations in key indicator species and the reconstructed chlorophyll-a were used to examine the impact of climate-driven glacier readvances in the mid-southern BIC foreland (Figure 4, 5). A notable shift in XRF-CS geochemistry exists at ~60 cm depth (Figure S1), but we found no clear bio-geochemical evidence of (glacio) marine sedimentation. Although diatom

concentration in the lowermost zone was too low for quantitative analysis, all sedimentary units younger than c. 6 cal. ka BP (~63 cm) contained freshwater diatoms. The $\delta^{13}C$ value from 73.5–74.5 cm depth is also consistent with a freshwater sedimentary environment, implying that it is younger than c. 6.5 cal. ka BP. The increase in diatom accumulation rate from c. 1.9 cal. ka BP is linked to the increased input of minerogenic sediments and dry mass accumulation rate between c. 1.9 and 1.6 cal. ka BP (Figure S8). Redundancy analysis (RDA) using key geochemical variables associated with tephra from XRF-CS analysis showed that tephra deposition did not have a significant impact on the diatom community composition in the Kiteschsee Lake record (p=0.596) (Figure S9, S10).

Using constrained cluster analysis (Figure 4A, S9), we divided the diatom record from 47 cm upwards into five zones (Supplementary Materials for details). Diatom Zones 4 and 5 are of most interest to this study because they correspond to a decline in aerophilic and littoral diatom species and concurrent increases in species associated with more turbid conditions (e.g., *Stauriserella pinnata*), and lower DCCA scores (Figure 4A, 5B, S9). The transition to increased minerogenic input in lithofacies Unit 8 coincides broadly with the start of Diatom Zone 4 (22–13 cm: 1.3–0.8 cal. ka BP). Trends initiated in Diatom Zone 4 continued in Zone 5 until ~5 cm depth (mid-late C20th onwards), when there was a significant shift to a subaquatic freshwater moss (*Drepanocladus longifolius* (Mitt. Paris) sp.) dominated environment (Lithofacies Unit 10).

[insert Figure 5.]

Discussion

In this section, we assess: 1) The Holocene deglaciation and glacial readvance history of the BIC, of KGI, and relationships to regional-global change; 2) Mechanisms driving Holocene climate-glacier dynamics on the AP identified in Bentley et al. (2009), principally, solar insolation, westerly winds, the Southern Annular Mode (SAM); 3) Impacts of Holocene deglaciation and glacier readvances.

Palaeoenvironmental history and change

Early Holocene deglaciation c. 12–8 cal. ka BP

Previously published lake sediment records show that the terrestrial deglaciation of the southern-mid part of the Fildes Peninsula from the LGM ice limit dates to c. 12–9 cal. ka BP (Mäusbacher et al., 1989; Watcham et al., 2011) (Figure 1), and was broadly coeval with other areas of the SSI (Palacios et al., 2020). New radiocarbon data from the BIC foreland and Potter Cove show the ice cap had thinned and retreated substantially during the early Holocene, with large parts of the Fildes Peninsula and Potter Peninsula becoming ice free by c. 8 cal. ka BP. The BIC had also retreated from the central area of Fildes Peninsula by c. 8 ka (Figure 1, 6A, 7E). New chronological evidence from the BIC foreland and the Shetland I moraine in this study is consistent with the deglaciation of Mondsee Lake (Figure 2), 45 m a.s.l., ~1,500 m away from the present glacier margin at this time (Schmidt et al., 1990). Recession progressed towards the higher elevation areas in the eastern sector, located above the C20th equilibrium line altitude (ELA) of ~150 m a.s.l., into areas located in depressions next to the former ice limit, and triggered an increased rate of isostatic uplift and falling relative sea level (Figure 7E, F) (Watcham et al., 2011).

[insert Figure 6.]

[insert Figure 7.]

We divided the eight probability 'gaps' that represent possible readvances on the Fildes Peninsula and on King George Island into four stages as follows: Stage 1: c. 7 ka readvance/standstill (7.4–6.6 cal. ka BP); Stage 2: Mid Holocene retreat followed by up to four possible minor readvances at 5.3–4.8 cal. ka BP; 4.5–3.9 cal. ka BP; 3.3–3.0 cal. ka BP; 2.6–2.2 cal. ka BP; Stage 3 readvance: 1.7–1.4 ka; Stage 4 readvances: 1.0–0.7 cal. ka BP and <0.7 cal. ka BP.

Stage 1 readvance/standstill

Using evidence from marine-freshwater transitions in isolation basins between 14–16 m a.s.l., Watcham et al. (2011) established a Holocene marine limit of ~16 m a.s.l. at c. 8.0 cal. ka BP and that the short-lived fall in RSL and return to that level at c. 7.0 cal. ka BP on the Fildes Peninsula was indicative of a restricted readvance or standstill in glacier retreat. New cosmogenic exposure ages from erratics in this study show the NW marine platform close to the present BIC ice front on the Fildes Peninsula became ice-free by c. 6.5 ka (Figure 7E, Table 1). We found no evidence for cosmogenic nuclide inheritance; therefore, the dated erratics had not been reworked or eroded from pre-Pleistocene formations on the SSI and were most likely

glacially transported from the AP prior to (or during) the LGM, then fully reset by glacial reworking prior to deglaciation. Our new data are consistent with isolation basin evidence for a restricted readvance/standstill at c. 7 cal. ka BP on the Fildes Peninsula and evidence of a marine transgression at c. 7.5–7.0 cal. ka BP in Potter Cove followed by a glacier readvance at <7.0 cal. ka BP on Potter Peninsula (Strelin et al., 2014) (Figure 3, 5A, 6A, 7E-G).

Based on previous geomorphological mapping (López-Martínez et al., 2012; Michel et al. 2014a) and the retention of snow patches even during late summer on some satellite imagery, parts of the Davies Heights were probably glaciated during the Stage 1 readvance and colder phases of the Holocene (Figure 6A, C).

New cosmogenic exposure ages and radiocarbon ages from bivalve shells in marine sediments from the Shetland I moraine dated to between 6.8 and 5.3 cal. ka BP (95% probability phase range; Figure 5A) constrain (renewed) deglaciation across the BIC foreland to <c. 7 cal. ka BP. Persistently warmer atmospheric temperatures across the Peninsula between 7 and 6 cal. ka BP is reflected in reduced sea-ice and warmer-than-Holocene-average sea-surface temperatures in marine sediment records from Maxwell Bay and the Palmer Deep between 8.2 and 5.9 cal. ka BP (Figure 5D) (Milliken et al., 2009; Mulvaney et al., 2012; Etourneau et al., 2013). Overall, the marine-terminating BIC was less extensive during this shell colonization phase between 6.8–5.3 cal. ka BP (Hall, 2007; Fretwell et al., 2010). Tiefersee Lake and Hochlandsee Lake, located ~800 and ~1500 m from the present-day ice cap, became ice free (Figure 2, 3E) as the BIC retreated to within its present-day limits by c. 6.0 cal. ka BP on land (Mäusbacher et al., 1989; Mäusbacher, 1991) and its marine-terminating glacier front (re)occupied the inner bays of Collins Harbour in Maxwell Bay (Tatur et al., 1999; Yoon et al., 2006; Milliken et al., 2009; Simms et al., 2011; Watcham et al., 2011; Chu et al., 2017), and at the same time as ice sheets and caps thinned, and ice shelves retreated elsewhere on the AP and around Antarctica (Roberts et al., 2008; Hein et al., 2016; Verleyen et al., 2017; Johnson et al., 2011, 2020).

Stage 2 Readvances c. 5.3–2.2 cal. ka BP

There are four probability 'gaps' when minor readvances could have occurred between c. 5.3–2.2 cal. ka BP (5.3–4.8 cal. ka BP, 4.5–3.9 cal. ka BP, 3.3–3.0 cal. ka BP and/or 2.6–2.2 cal. ka BP). Evidence for glacier readvances on KGI and SSI is limited across the mid- to late Holocene transition, but it seems likely that the general warming transition into the mid Holocene Hypsithermal (MHH) as defined by Bentley et al. (2009) (now referred to as the

Holocene Hypsithermal, HH) was interspersed by at least one short-lived or restricted readvance (Figure 3D, 5).

Marine sediments and bivalve shells dated to between 6.8 and 5.3 cal. ka BP were reworked into till at the extreme east of the Shetland I moraines most likely between 5.3–3.9 cal. ka BP as RSL fell below 15 m a.s.l. (Figure 2, 6B, 7E; Table 2, S3), but we found no evidence of BIC readvance on the Fildes Peninsula beyond its present-day limits at this time. Moraines were located close to the former sea-level prior to reworking, and Holocene raised beaches up to ~16–18 m a.s.l. extended under the BIC in the Artigas Beach area may have survived relatively unmodified beneath the ice cap (John and Sugden, 1971; Hall, 2003).

A Stage 2 readvance probability 'gap' between 5.3–4.8 cal. ka BP (Figure 5A) overlaps with persistently colder temperatures in the Yanou Lake GDGT-temperature record between 6.0–3.7 cal. ka BP as well as a hypothesised local readvance in the Stranger Point area of Potter Peninsula at c. 5 cal. ka BP (Emslie et al., 2019) and glacier readvances elsewhere on the NAP (Figure 5C, F, I). Surface temperatures decreased. Sea-ice cover also increased in Maxwell Bay between c. 5.9 and 2.6 cal. ka BP and summer sea-ice occupied the inner Collins Harbour of Maxwell Bay until at least c. 1.7 cal. ka BP (Simms et al., 2011).

In contrast, on land, warmer-than-Holocene-average atmospheric temperatures across the SSI and AP between c. 6.0 and 2.8 cal. ka BP led to extensive moss banks and the formation of widespread lacustrine subaquatic moss layers on KGI (Figure 3E, 5F) (Björck, 1991a; Björck, 1991b; Sun et al., 2005; Hall, 2007; Bentley et al., 2009; Mulvaney et al., 2012; Foster et al., 2016; Yu et al., 2016; Roberts et al., 2017). Subaquatic freshwater moss was occasionally present in most lakes on Fildes Peninsula between 6.0–3.0 cal. ka BP (Watcham et al., 2011; Roberts et al., 2017) (Figure 3E, 5A).

Stage 3 readvance (Late Holocene Neoglacial) c. 1.7–1.3 ka

The BIC readvanced only by tens of metres relative to its present position in the Artigas Beach area in the second half of the Late Holocene and most of the present-day Shetland I moraine was established during Stage 3 and/or Stage 4 readvances.

New mean radiocarbon ages from moss fragments incorporated into a small moraine on top of a raised beach at 7–6 m a.s.l. on Artigas Beach, indicate a two stage readvance of the BIC in this area during the late Holocene: the first, after the formation of the raised beach and

sometime between c. 1.7 and 1.4 cal. ka BP (Stage 3 readvance) and a second at <0.7 cal. ka BP (Stage 4 readvances). New radiocarbon ages also constrain the initial formation of the present-day Shetland I moraine from Valle Norte towards its eastern extension (see Figure 2 for location), where moraines are still ice-cored and in contact with the present ice. There, we found moraine crests several meters above the ice-level, similar to those found in Valle Norte (Hall, 2007), which post-date c. 1.2 cal. ka BP, the age of the youngest new sample dated. This age means that the eastern part of the BIC was landward of its present limit, with mosses colonizing its foreland until at least 1.2 cal. ka BP.

The Stage 3 readvance occurred after the start of the 'Neoglacial' on the AP, defined as 2070 ± 50 cal a BP by Čejka et al. (2020). The most significant downturn in the Yanou Lake reconstructed GDGT-temperature record occurred at c.1.3 cal. ka BP and coincided with a shift to more turbid conditions in Kiteschsee Lake (Figure 5B, C, S11). The Davies Heights could have been ice-covered at this time, even with a relatively minor reduction in temperature as they are close to the present-day ELA (Figure 6C). The Stage 3 readvance was broadly synchronous with two phases of glacier expansion and the reformation of ice shelves on the north-eastern AP (Figure 5F), and in Southern South America between c. 1.5 and 1.1. cal. ka BP (Balco and Schaefer, 2013; Strelin et al., 2014; Moreno et al., 2018; Kaplan et al., 2020) and occurred when a colder conditions existed on the north-eastern AP (Figure 5G) (Mulvaney et al., 2012), but also when composite ice core records from elsewhere in Antarctica show a predominantly warmer phase (Masson et al., 2000).

Stage 4 readvance(s) c. 1.0–0.7 cal. ka BP and after <0.7 cal. ka BP

Probability 'gaps' in the Shetland I moraine radiocarbon ages (Figure 3) suggest that readvances could have occurred at c. 0.7, 0.4 and/or <0.2 cal. ka BP. Hall (2007) determined that glacier readvances of the Shetland I moraines occurred at Valle Norte and Valle Klotz (Figure 1 for locations) between c. 1.0 and 0.7 cal. ka BP (Figure 2, 3C, 5A). Ice in these areas advanced in lobes, which spread out into ice-marginal depressions, forming several small thrust moraines, ~300 m from the prominent moraine ridges (dated in this study). These ages broadly align with persistently low DCCA Axis 1 (β-diversity) values in Diatom Zone 5 of Kiteschsee Lake, reflecting resuspension of sediment in a more persistently-turbid lake environment, indicative of reduced lake ice, increased meltwater and/or stronger winds (Figure 4, 5B, S5F, S11). We found no new chronostratigraphic data constraining a readvance <1 cal. ka BP, but Hall (2007) described the 'last readvance' at <0.2 cal. ka BP as the most extensive phase of glacier readvance of the last c. 3,500 years.

The Stage 4 readvances, and increased lake turbidity, occurred during a phase of sustained colder reconstructed summer air temperatures in the nearby Yanou Lake record (Figure 5C, S11) (Roberts et al., 2017) after the Medieval Climate Anomaly (MCA) (c. 1.2 and 0.8 cal. ka BP - Bentley et al. (2009); 1250–950 CE - Mann et al. (2009). No evidence of substantial glacial readvance exists on KGI or the northern AP during the MCA (Charman et al., 2018; Emslie et al., 2019; Oliva et al., 2019; Kaplan et al., 2020), and marine sediment records from Maxwell Bay and Potter Cove imply no substantial increases in sea-ice at this time (Figure 5D) (Milliken et al., 2009; Monien et al., 2011). Increased fine-grained sedimentation in Potter Cove during the MCA has been linked to warmer conditions, including warmer sea surface temperatures from the western AP (Milliken et al., 2009; Hass et al., 2010; Watcham et al., 2011; Etourneau et al., 2013). Some Southern Hemisphere proxy records between 60 and 90°S (Figure 5H) show warmer conditions during the MCA (Marcott et al., 2013; Neukom et al., 2014; Kaufman et al., 2020a, b), but no sustained upturn in temperature exists in the James Ross Island ice core record or the Yanou Lake GDGT palaeotemperature record during the MCA (Figure 5C, S11, S12) (Björck et al., 1993; Mulvaney et al., 2012; Roberts et al., 2017; Kaplan et al., 2020).

The final probability gap (readvance) after <0.2 ka is broadly synchronous with geomorphological and sedimentological evidence for glacier advance on Potter Peninsula/Cove (Hass et al., 2010; Heredia Barión et al., 2023), elsewhere on the SSI, the AP and several sub-Antarctic islands (Hall and Perry, 2004; Bentley et al., 2007; Hall, 2007; Bentley et al., 2009; Hall, 2010; Roberts et al., 2010; Davies et al., 2014; Guglielmin et al., 2016; van der Bilt et al., 2017; Simms et al., 2021; Verfaillie et al., 2021), extreme cold 'events' in most Southern Hemisphere palaeorecords (Neukom et al., 2014), and the Northern Hemisphere 'Little Ice Age' (0.55–0.25 cal. ka BP, 1,400-1,700 CE) (Mann et al., 2009; Kaufman et al., 2020a, b).

Mechanisms of Holocene climate-glacier dynamics

Deglaciation of the Fildes Peninsula and other peninsulas on KGI to present day limits occurred in two broad phases during the early-mid Holocene. The first phase between c. 15 and 8 cal. ka BP occurred during a period of rising spring/summer insolation at 62 °S and relatively elevated global solar irradiance in the transition into the present (Holocene) interglacial (Figure 7A, D, E) (Steinhilber et al., 2009; Baggenstos et al., 2019; Reynhout et al., 2019). This coincided with a period of sustained warmth and persistently positive Southern Annular Mode

(SAM)-like conditions (Figure 7D). Meanwhile, data from the BIC foreland moraines and other readvance constraints across KGI suggest that ice caps on the SSI likely responded to millennial- to centennial-scale changes in solar forcing (insolation and irradiance), westerly wind strength and the SAM in the mid-late Holocene.

The SAM is the primary mode of annual to centennial scale variability in atmospheric circulation in the Southern Ocean (Marshall, 2007) and reflects the zonal mean sea level pressure difference between Antarctica (>65°S) and the mid latitudes (40°S); hence, the SAM index is, in effect, a measure of the longitudinal mean SHW strength (Marshall, 2007). Positive SAM phases are associated with lower pressure at higher latitudes, more poleward focussed SHW, with stronger Westerlies in summer and stronger Easterlies in winter over the NAP and SSI (Martin et al., 2021). During the Holocene, stronger and more poleward SHW are thought to be the centennial- to millennial-scale expression of decadal-centennial warming and positive SAM-like conditions (Charman et al., 2018; Moreno et al., 2018, 2021; Perren et al., 2020). Conversely, phases of enhanced El Niño drive warmer interannual global mean temperature variability and negative phases of the SAM, which are characterised by colder and more humid conditions on the NAP, SSI and sub-Antarctic islands, and have increased over the last 4 kyr (Figure 7C) (Wang and Cai, 2013; Turner et al., 2016; Reynhout et al., 2019; Kaplan et al., 2020; Verfaillie et al., 2021).

Since 1957 CE, the longer-term pattern of interannual variability in the SAM has been altered by the ozone hole over Antarctica, which, combined with increased greenhouse gases and global temperature, has led to more positive SAM-like conditions, similar to the early Holocene, and enhanced the ENSO (Marshall, 2007) (Figure 7D). Increased cyclonic activity in the Drake Passage between 1996–2005 CE has been linked to a more poleward focussed SHW and more positive SAM, driving sea-ice poleward and increasing the advection of warm air across the NAP and SSI during winter (Oliva et al., 2017; Marshall et al., 2017). Between 2006–2015 CE colder winters pushed sea ice north, increasing snowfall across the NAP and doubling snow cover on some SSI islands between 2009–14 CE (Oliva et al., 2017; de Pablo et al., 2013). In addition, the SAM and a deepening Amundsen Sea low have been interacting in recent decades, bringing warmer air from the Atlantic and north-easterly winds with cooler air from the Weddell Sea (Liu et al., 2005; Davies et al., 2014; Kaplan et al., 2020). As a result, the NAP and SSI became colder and wetter, and its glaciers have gained mass (Thomas et al., 2008; Goodwin et al., 2016; Oliva et al., 2017; Falk et al., 2018).

Accordingly, longer-term changes in temperature and precipitation that drove glacier readvances on the NAP and SSI during the Holocene were most likely the result of annual to millennial scale variations in the position and intensity of the SHW, modulated by changes in the SAM (Moy et al., 2008; Bentley et al., 2009; Lamy et al., 2010; Varma et al., 2012).

The Stage 1 readvance occurred during a downward trend in global solar irradiance between c. 7.5 and 7.0 cal. ka BP which coincided with the transition to colder and more negative SAM-like conditions as the SHW migrated marginally equatorward (Figure 7A–C, G). Glacier readvance(s) on KGI are regionally coherent with readvances on the eastern AP (Kaplan et al., 2020; Figure 5F) and in Patagonia at c. 7 ka (Strelin et al., 2014; Reynhout et al., 2019), implying a common forcing mechanism.

Following the Stage 1 readvance, increasing spring/summer insolation over the SSI and global solar irradiance, weaker or marginally equatorward westerlies, and reduced storminess drove glacier retreat on the Fildes Peninsula and the Potter Peninsula between c. 6.6–5.3 cal. ka BP. (Figure 7A-D, G, H) (Bentley et al., 2009; Quade and Kaplan, 2017; Saunders et al., 2018; Reynhout et al., 2019; Heredia Barión et al., 2023). Retreat on KGI coincided with sustained temperatures around the 0-12 ka mean in the Southern Hemisphere high latitudes and with the 'Holocene global thermal maximum', centred on 6.5–6.0 cal. ka BP (Figure 5H). Although the latter is more clearly defined in Northern Hemisphere proxy records, average global temperatures were 0.7 °C warmer than the 'pre-industrial' reference period, defined by the IPCC as 1850–1900 CE (Kaufman et al., 2020a, b). Windier conditions further north at this time in the Southern Ocean have been linked to rising temperatures (Marcott et al., 2013; Saunders et al., 2018; Kaufman et al., 2020a, b) (Figure 5H, 7B, 7C).

While transitions into and/or out of short-lived phases of marginally more positive SAM-like conditions in the Mid- to Late Holocene could have increased snow accumulation on the SSI, the combination of generally colder and more negative SAM-like conditions, stronger westerly winds, and an enhanced ENSO from c. 4 ka onwards (Garreaud, 2007; Yang et al., 2019) led to deteriorating regional climatic conditions that lowered the ELA across the SSI and drove Late Holocene Stage 2, 3, and 4 readvances on KGI (Figure 5C,G, 7A-D, G, H, S12).

Stage 3 and 4 readvances occurred as spring/summer insolation at 62°S declined and around global irradiance minima in the last 2,000 years and during persistently colder conditions in lake records from the mid-outer areas of the Fildes Peninsula (Figure 5C) (Roberts et al., 2017).

Late Holocene readvances are anti-phased with aquatic moss layers in lake records from outer Fildes Peninsula lakes that were not directly affected by glaciofluvial inputs. Generally stronger westerly winds and colder/more negative SAM-like conditions likely drove marginal increases in snow accumulation and greater turbidity in Kiteschsee Lake (Figure 4, 5B, 7B), but an equatorward shift in the core westerly wind belt storm belt to <55°S likely reduced storminess (and precipitation), restricting readvances to around or within present day limits (Figure 4, 5B, 7B, 7C).

From the mid-late C20th onwards, the mode of sedimentation in Kiteschsee Lake, other lakes on the mid-outer Fildes Peninsula and lakes elsewhere on King George Island that are now detached from direct glaciofluvial influence has shifted dramatically to one dominated by sub-aquatic moss (Figure 4A, S1). We link this dramatic ecological shift to the Recent Rapid Regional warming (RRR) on the northern AP and SSI (Bentley et al., 2009) and increasingly positive SAM-like conditions that have moved stronger SHW poleward in the late C20th and early C21st (Figure 7D), associated with anthropogenic activity (e.g., the ozone hole, increasing greenhouse gas emissions).

Impacts of Holocene deglaciation and glacier readvances

Relative sea level change is the most obvious impact of ice (un)loading on the SSI during the Holocene. Data constraining RSL change on the SSI following deglaciation are more complex than other locations across Antarctica, and several different RSL curves have been suggested (Pallàs et al., 1997; Bentley et al., 2005; Hall, 2010; Roberts et al., 2011; Watcham et al., 2011; Simms et al., 2012; 2021; Johnson et al., 2022). Bentley et al. (2005) initially proposed that RSL declined from an undated Early-Mid Holocene marine limit of ~16–18 m a.s.l. in a discontinuous manner as the SSI deglaciated, and was interrupted at 14.5–16 m a.s.l. by a readvance between 5.8–3.0 cal. ka BP. In contrast, and with more data, Hall (2010) and Watcham et al. (2011) both suggested RSL fell continuously after 6 cal. ka BP, implying glacier readvances were restricted and had limited isostatic impact.

A readvance/standstill at c. 7 ka is consistent with evidence of marine-freshwater transitions in isolation basins between 14–16 m a.s.l. on the Fildes Peninsula (Watcham et al., 2011). There is limited evidence for RSL change associated with Stage 2 readvance(s), but some Stage 3 and 4 readvance(s) have been linked to increased isostatic rebound followed by an accelerated rate of RSL decline between 1.5–0.5 ka BP (Figure 7F) (Simms et al., 2012; Johnson et al., 2022). Raised beaches at <10 m a.s.l., are thought to be contemporaneous with Late Holocene

readvances on KGI and Livingston Island between c. 0.5 and 0.25 cal. ka BP (Sugden and John, 1973; Hall and Perry, 2004; Hall, 2010). Restricted Late Holocene readvances on the Fildes Peninsula are consistent with the limited Late Holocene ice-loading scenario of the W12a GIA model (Whitehouse et al., 2012a, b). Greater 'Neoglacial' ice-loading is broadly supported by field data, implying more substantial readvances and/or differential ice-mass (un)loading elsewhere on the SSI during the Late Holocene (cf. Fretwell et al., 2010).

Thick airfall tephra layers and >0.5 m thick gravity flow deposits in lake sediments from across the SSI dated to between c. 5.6–3.8 cal. ka BP have been linked to the Deception Island caldera-forming event (Figure 5C) (Roberts et al., 2017; Antoniades et al., 2018; Supplementary Material for details). Interestingly, rhyolitic tephra associated with the three most explosive Deception Island eruptions of the Holocene (T7, T5, CC in Figure 5C) has been found in lake sediments from Fildes Peninsula shortly after the BIC had deglaciated close to/within its present-day limits at c. 8.0–7.5 cal. ka BP (T7: 6.5-7.2 cal. ka BP), after c. 6.0 cal. ka BP (T5: 5.2-5.6 cal. ka BP), and after the c. 4.2 cal. ka BP readvance (CC: 3.98±0.13 cal. ka BP) (Table S1B; Supplementary Material for details). More than one Deception Island caldera-forming event in the Holocene is considered unlikely due to the amount of time needed to fully recharge the magma chamber (Geyer et al., 2019). Instead, explosive (rhyolitic) eruptions from Deception Island generated by magma injection processes (Geyer et al., 2019) could have been triggered by increased crustal and magma chamber stress, associated with isostatic rebound, and increased magma interaction with sea water, associated with localised changes in sea level, during the Mid- to Late Holocene (cf. Maclennan et al., 2002; Forte and Castro, 2019; Satow et al., 2021; Praetorius et al., 2016). Further work is needed on the South Shetland Islands to investigate the relationship between Holocene deglaciation and volcanic activity.

Conclusions

We reconstructed the Mid- to Late Holocene deglaciation and readvance history of the Fildes Peninsula, King George Island/Isla 25 de Mayo (KGI), South Shetland Islands, NW Antarctic Peninsula, using new cosmogenic exposure ages from glacial erratics on the foreland of the Bellingshausen Ice Cap (BIC), radiocarbon dating of terrestrial mosses and marine *Laternula* sp. bivalve shells found in moraines on the Artigas Beach and Valle Norte sectors of BIC foreland.

Deglaciation on KGI began after c. 15 ka and had progressed to within present-day limits on the Fildes Peninsula, its largest ice-free peninsula, between c. 6.6–5.3 cal. ka BP as

spring/summer insolation at 62°S gradually increased, leading to generally warmer and more positive SAM-like conditions during the early Holocene.

Using a novel statistical approach, we developed a new deglaciation and four-stage Holocene readvance model for the BIC on the Fildes Peninsula.

Probability density phase analysis of new (n=25) and existing chronological data constraining Holocene glacier advance on the Fildes Peninsula and other ice-free peninsulas of KGI (n=80 in total) revealed up to eight 95% probability 'gaps' when readvances could have occurred, which we grouped into four stages:

- **Stage 1**: a readvance and marine transgression, well-constrained by field data, between c. 7.4–6.6 cal. ka BP.
- **Stage 2**: four less well-constrained readvance probability 'gaps' between c. 5.3–4.8 cal. ka BP, 4.5–3.9 cal. ka BP, 3.3–3.0 cal. ka BP and 2.6–2.2 cal. ka BP.
- **Stage 3**: a well-constrained readvance between c. 1.7–1.5 cal. ka BP when terrestrial mosses were embedded in the Shetland I moraine and the BIC extended landward of its present position on its eastern flank.
- **Stage 4**: two further readvances, one less well-constrained by field data between c. 1.3–0.7 cal. ka BP (68% probability) when moss fragments and Mid-Holocene marine sediments were translocated into the moraines surrounding the present-day BIC and a prolonged phase of elevated turbidity existed in Kiteschsee Lake, and then a well-constrained 'final' readvance after <0.7 cal. ka BP, consistent with the 'last readvance' on James Ross Island, NE Antarctic Peninsula.

Similarities in the timing of Mid- to Late Holocene glacier readvances on the SSI, the northern Antarctic Peninsula, some sub-Antarctic Islands and in southern South America imply underlying regional-hemispheric drivers were responsible.

The Stage 1 readvance occurred at the Holocene global solar irradiance minimum as colder/more humid (negative) Southern Annular Mode (SAM)-like and stormier conditions developed, with marginally stronger (poleward shifted) westerly winds over the SSI.

Readvances were more frequent after c. 5.3 cal. ka BP, driven by reducing spring/summer insolation at 62°S and more persistent negative SAM-like conditions. However, weaker

(equatorward shifted) westerlies and reduced storminess over the SSI restricted readvances close to present day limits.

Late Holocene readvances occurred around global solar irradiance minima and are anti-phased with aquatic moss layers in lake records from outer Fildes Peninsula lakes unaffected by glaciofluvial inputs.

Recovery from Late Holocene 'Neoglacial' conditions in Kiteschsee Lake and other mid-outer lakes on the Fildes Peninsula in the post-bomb era (>1950 CE) is characterised by the recolonisation of well-developed aquatic moss at the lake sediment-water interface. This was driven by late 20th Century/early 21st Century warming of the northern Antarctic Peninsula and more positive SAM-like conditions on KGI.

Acknowledgements

We thank the crews of the Uruguayan research station "Artigas", the Russian Bellingshausen Station, the Chinese Great Wall Station, Base Presidente Eduardo Frei Montalva, the Argentine research station "Carlini" and the adjoined German Dallmann-Labor (AWI) Laboratory, the Brazilian Navy Almirante Maximiano, the UK Royal Navy HMS Endurance and the RRS James Clark Ross for their cordial hospitality and invaluable logistical support during the 2006, 2011 and 2015 field seasons. Fieldwork assistance was from Magnus Makeschin, Bulat Mavlyudov, Eliseo Flores, Marco Petit, Dirk Mengedoht, and Bruce Maltman, laboratory technical assistance was from Anke Toltz and Ruben Rosenkranz at the University of Cologne (sample processing for ^{10}Be exposure ages). We thank Laura Gerrish and Huw Griffiths (BAS) for assistance with GIS/map production. Alex Simms, Daniel Nývlt and an anonymous reviewer are thanked for their constructive comments on the original manuscript. This paper is dedicated to the memory of Doris Abele, an inspirational scientist and a good friend who led the IMCOAST and IMCONet Research Programs.

Funding

This study was funded by Centro de Investigaciones en Ciencias de la Tierra (CICTERRA), the Dirección Nacional del Antártico/ Instituto Antártico Argentino (DNA/IAA) in the framework of the Project PICTA, 2011 – 0102, IAA "Geomorfología y Geología Glaciar del Archipiélago James Ross e Islas Shetland del Sur, Sector Norte de la Península Antártica", granted to JS and support by the Alfred Wegener Institute (AWI), Helmholtz Centre PACES II (Polar Regions and Coasts in the changing Earth System). PHB, SR, EP, JS and GK were

funded by IMCONet (FP7 IRSES, action no. 319718) led by Doris Abele (AWI); LF by a NERC PhD Studentship NE/J500173/1 to BAS/Newcastle University. RM was supported by ANID R20F0002 (PATSER). EP, SR received additional funding from the Natural Environment Research Council (NERC/BAS-CGS Grant no.81). SR, DH, EH, MB were funded by the NERC/BAS science programmes CACHE-PEP: Natural climate variability – extending the Americas palaeoclimate transect through the Antarctic Peninsula to the pole to DH and GRADES-QWAD: Quaternary West Antarctic Deglaciations to MB (terrestrial), Carol Pudsey, Rob Larter (marine).

Author Contributions

PHB and SR designed the research and wrote the manuscript, constructed figures and tables with assistance from JD, IG, MB, GK; PHB, SR, EP, MB, DH, EH undertook fieldwork/sample collection. PHB and SB produced cosmogenic nuclide dating data; while CS provided ^{10}Be exposure dating analytical facilities; PHB, LW, GK, SR, MB undertook radiocarbon dating. Kiteschsee Lake core data and interpretations were undertaken by SR, EP, SD (ITRAX-XRF), JD, VJ (diatom analysis) IG, SB, RM, CH (tephra counting, geochemical identification of tephra layers); PHB, SR, CS, SB, GK, EP, MB, JS edited initial drafts and all authors read and commented on the final version. The authors declare no competing interests.

Data availability

Datasets generated in this study are included in the main text and Supplementary Materials and are available the NERC EDS UK Polar Data Centre (https://www.bas.ac.uk/data/uk-pdc/) and on request from polardatacentre@bas.ac.uk and sjro@bas.ac.uk. Code, data, and package references are also available on https://github.com/stever60/Fildes_Peninsula. Final figure layouts and additional annotations were produced using Adobe Illustrator CC v.2021 or CorelDRAW v.2020. Supplemental material for this article is available online https://doi.org/10.6084/m9.figshare.21352569

Figures

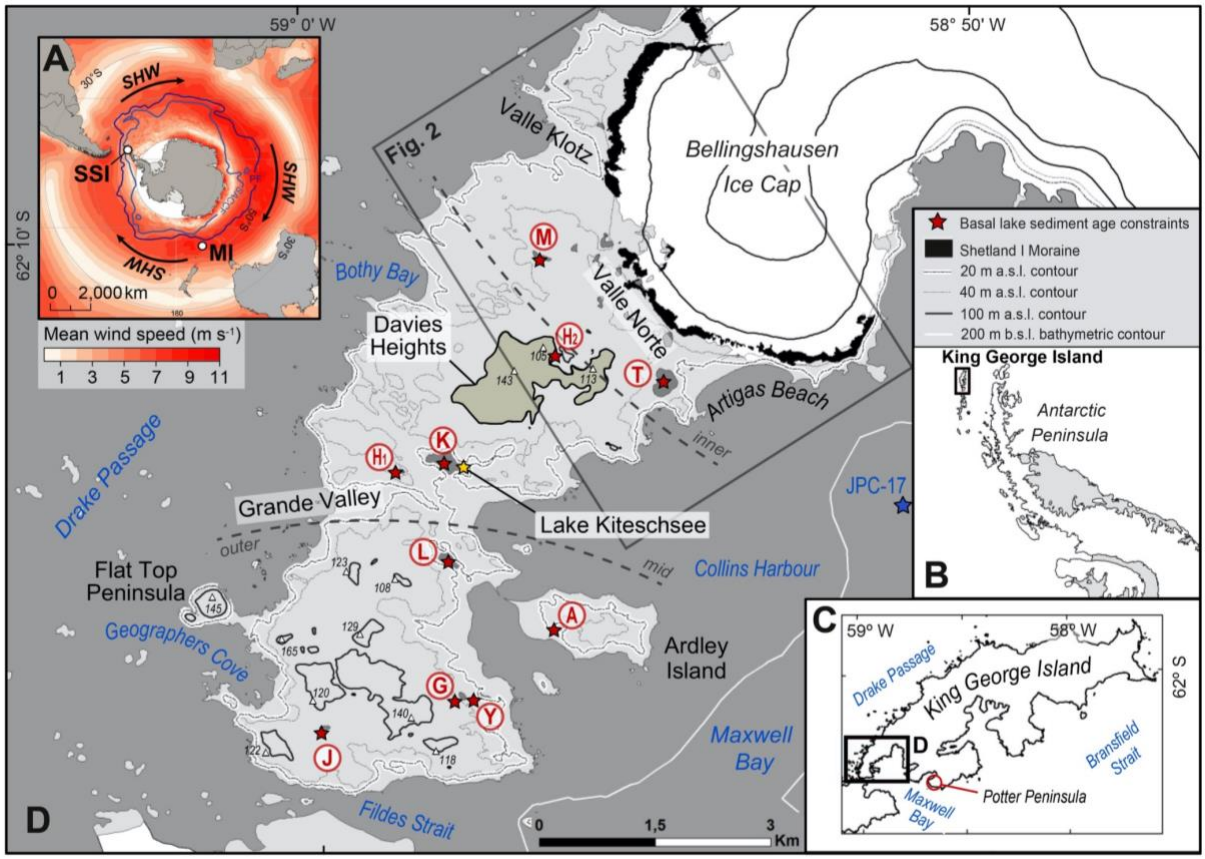

Figure 1. Geographic location of the study area. A) Location of the South Shetland Islands (SSI), currently south of the core Southern Hemisphere westerly Wind (SHW) belt. MI is Macquarie Island, located within the core SHW belt. B) Location of King George Island (KGI), South Shetland Islands on the north-western Antarctic Peninsula. C) KGI is framed by the Drake Passage and the Bransfield Strait. Box marks the position of the Fildes Peninsula. D) Map of the Fildes Peninsula showing minimum ages (cal a BP) for the onset of lake and offshore sedimentation. The Fildes Strait separates the Fildes Peninsula from Nelson Island, with Maxwell Bay to the east, and the open waters of the Drake Passage on its west coast. Lake record basal deglaciation ages (cal a BP ± 2σ), updated to Sh20/Marine20 for this study are as follows: Outer: J-Jurasee Lake (9,750±780 cal. a BP) (Mäusbacher et al., 1989), Y-Yanou Lake (10,830±340 cal. a BP) (Watcham et al., 2011; Roberts et al. 2017), G-Gaoshan Lake (7,250±120 cal. a BP) (Watcham et al., 2011), A-Ardley Lake (8,310±120 cal. a BP) (Watcham et al., 2011; Roberts et al., 2017), L-Long Lake (>6,480±180 cal. a BP) (Yoon et al., 2006; Watcham et al., 2011); Mid: Marine core JPC-17 (5,800 cal. a BP) (Simms et al., 2011), K-Kiteschsee Lake (>7,300±120 cal. a BP) (this study and Mäusbacher, 1991), H_1-Hotel Lake (6,960±150 cal. a BP) (Tatur et al., 1999), H_2-Hochlandsee Lake (6,150±400 cal. a BP) (Mäusbacher, 1991); Inner: T-Tiefersee (Profound) Lake (6,120±360 cal. a BP) and M-

Mondsee Lake (8,000±480 cal. a BP) (Schmidt et al., 1990). Contour lines: Antarctic Digital Database (http://www.add.scar.org/home/add7); bathymetry: GEBCO (Weatherall et al., 2015); spot heights (white triangles): Servicio Geográfico Militar de Uruguay.

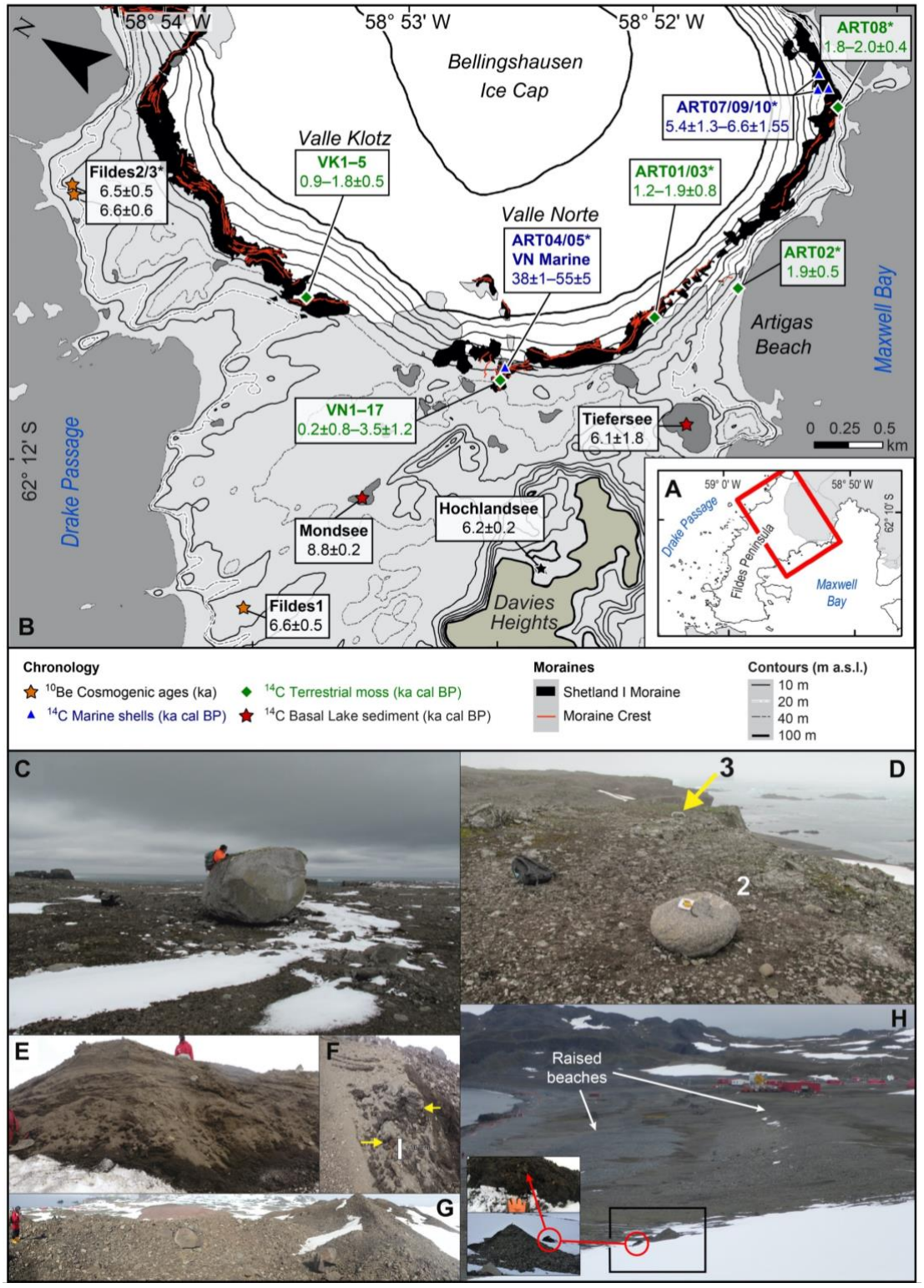

Figure 2. A–B) Map showing the position of cosmogenic ^{10}Be exposure ages of sampled erratics (orange stars) and calibrated radiocarbon ages of organic remains in the Shetland I moraine (black shading) and minimum ages of the onset of lake sedimentation (red stars). Inset map shows the area where the study sites are located (red box). BIC is Bellingshausen Ice Cap. VK = Valle Klotz, VN = Valle Norte, both sampled and dated by Hall (2007); asterisks indicate new data in this study. C–F) Field photographs showing the erratics sampled on the NW marine platform for terrestrial cosmogenic nuclide exposure age dating and terrestrial sediments preserved within the Shetland I moraine. C) Fildes 1 and D) Fildes 2 and 3 boulders sampled for cosmogenic analysis. Boulder dimensions and locations are in Table 1. E & F) Radiocarbon dating samples from locations ART-01 and ART-03 embedded in moraine sediments (Table 2). G) View from the crest of the Shetland I moraine in the Artigas Beach ART01/03 area looking approximately south towards the Uruguayan Station. H) The small moraine on top of a raised beach at 7–6 m a.s.l. on Artigas Beach at ART02 (open black box) and inset close ups of the moraine and ART02 reworked moss deposits sampled (red circles), looking approximately SW towards the Uruguayan Artigas Station, with the Davies Heights beyond.

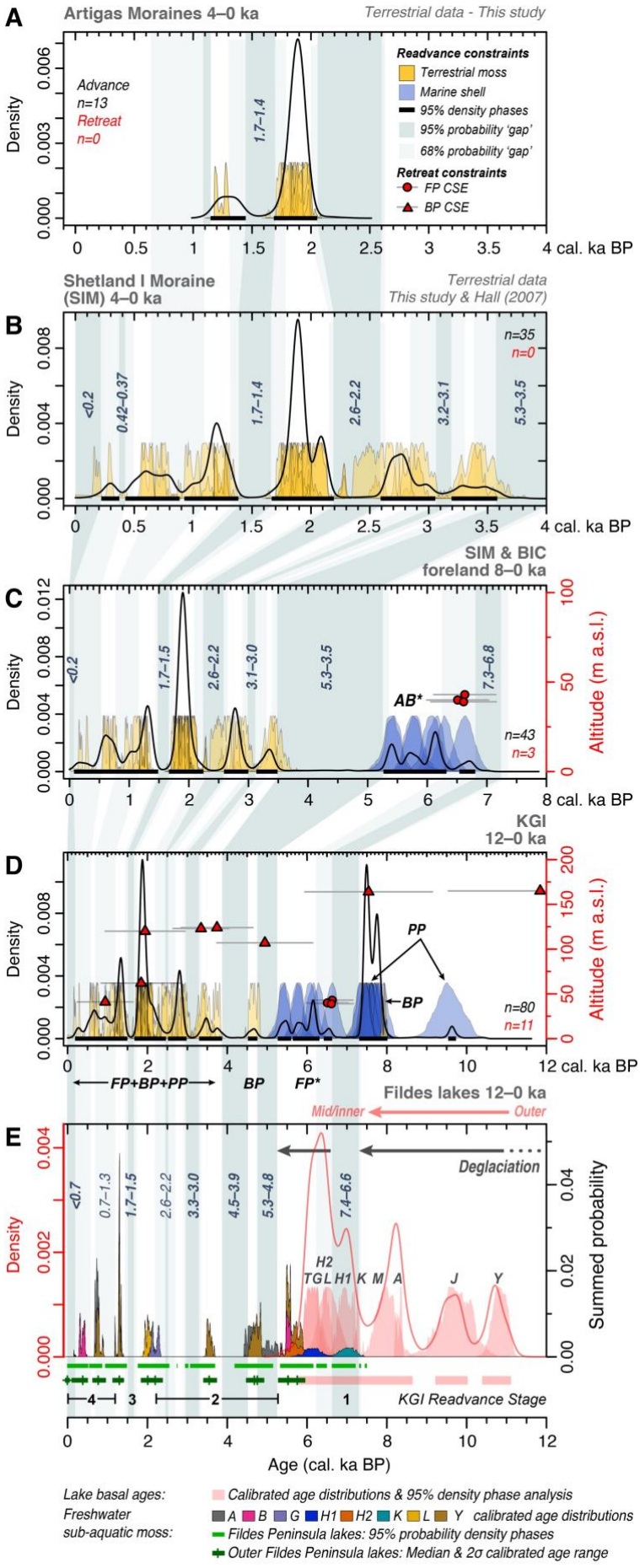
A
Artigas Moraines 4–0 ka
Terrestrial data - This study
Density
Advance
n=13
Retreat
n=0
1.7–1.4
Readvance constraints
Terrestrial moss
Marine shell
95% density phases
95% probability 'gap'
68% probability 'gap'
Retreat constraints
FP CSE
BP CSE
4 cal. ka BP
B
Shetland I Moraine
(SIM) 4–0 ka
Terrestrial data
This study & Hall (2007)
n=35
n=0
<0.2
0.42–0.37
1.7–1.4
2.6–2.2
3.2–3.1
5.3–3.5
4 cal. ka BP
C
SIM & BIC
foreland 8–0 ka
<0.2
1.7–1.5
2.6–2.2
3.1–3.0
5.3–3.5
7.3–6.8
AB*
n=43
n=3
Altitude (m a.s.l.)
8 cal. ka BP
D
KGI
12–0 ka
PP
BP
n=80
n=11
FP+BP+PP
BP
FP*
12 cal. ka BP
Fildes lakes 12–0 ka
Mid/inner
Outer
E
Deglaciation
<0.7
0.7–1.3
1.7–1.5
2.6–2.2
3.3–3.0
4.5–3.9
5.3–4.8
7.4–6.6
H2
TGL H1 K M A
J
Y
Summed probability
KGI Readvance Stage
Age (cal. ka BP)
Lake basal ages:
Calibrated age distributions & 95% density phase analysis
Freshwater sub-aquatic moss:
A B G H1 H2 K L Y calibrated age distributions
Fildes Peninsula lakes: 95% probability density phases
Outer Fildes Peninsula lakes: Median & 2σ calibrated age range

Figure 3. A) Radiocarbon ages and probability density phase model (black bars 95%) for terrestrial mosses dated in this study from the Artigas Beach sector moraines between 4–0 cal. ka BP (i.e., sample locations ART01–03 only in Figure 2; maximum age constraints on readvance). Dark and light grey shaded zones, with 95% probability timings, indicate periods when glacier readvances could have occurred (95% and 68% probability, respectively). B) Combined radiocarbon ages and probability density phase model for terrestrial mosses dated in this study from the Artigas Beach sector moraines and the Valle Norte–Valle Kotz sector moraines dated by Hall (2007) shown in Figure 2A; all data are maximum age constraints on readvance. C) Radiocarbon ages and probability density phase model for the Shetland I moraine 8–0 cal. ka BP, consisting of terrestrial mosses from this study and Hall (2007) and marine shells dated from the Artigas Beach (AB*) sector moraines in this study. Cosmogenic surface exposure (CSE) ages from the BIC foreland from this study are also shown (red circles; minimum age constraints on retreat). D) Probability density phase model for all maximum age constraints on glacier readvance on King George Island between 12–0 cal. ka BP. Cosmogenic nuclide exposure ages from this study (red circles) and Barton Peninsula (Seong et al., 2008) (red triangles) provide minimum constraints on retreat. BP=Barton Peninsula; FP=Fildes Peninsula, PP=Potter Peninsula. E) Probability density phase model for basal deglaciation ages (red line and bars) compared to a summed probability density profile of radiocarbon ages from subaquatic freshwater moss layers in lake sediment records from the Fildes Peninsula. King George Island (KGI) Readvance Stages 1–4 are also shown. Subaquatic freshwater moss layer deposition represents lacustrine conditions similar to the present day. Lakes are as shown in Figure 1; units for the probability density phase analysis are cal. ka BP^{-1}; data sources are shown in subtitles and described in code input files.

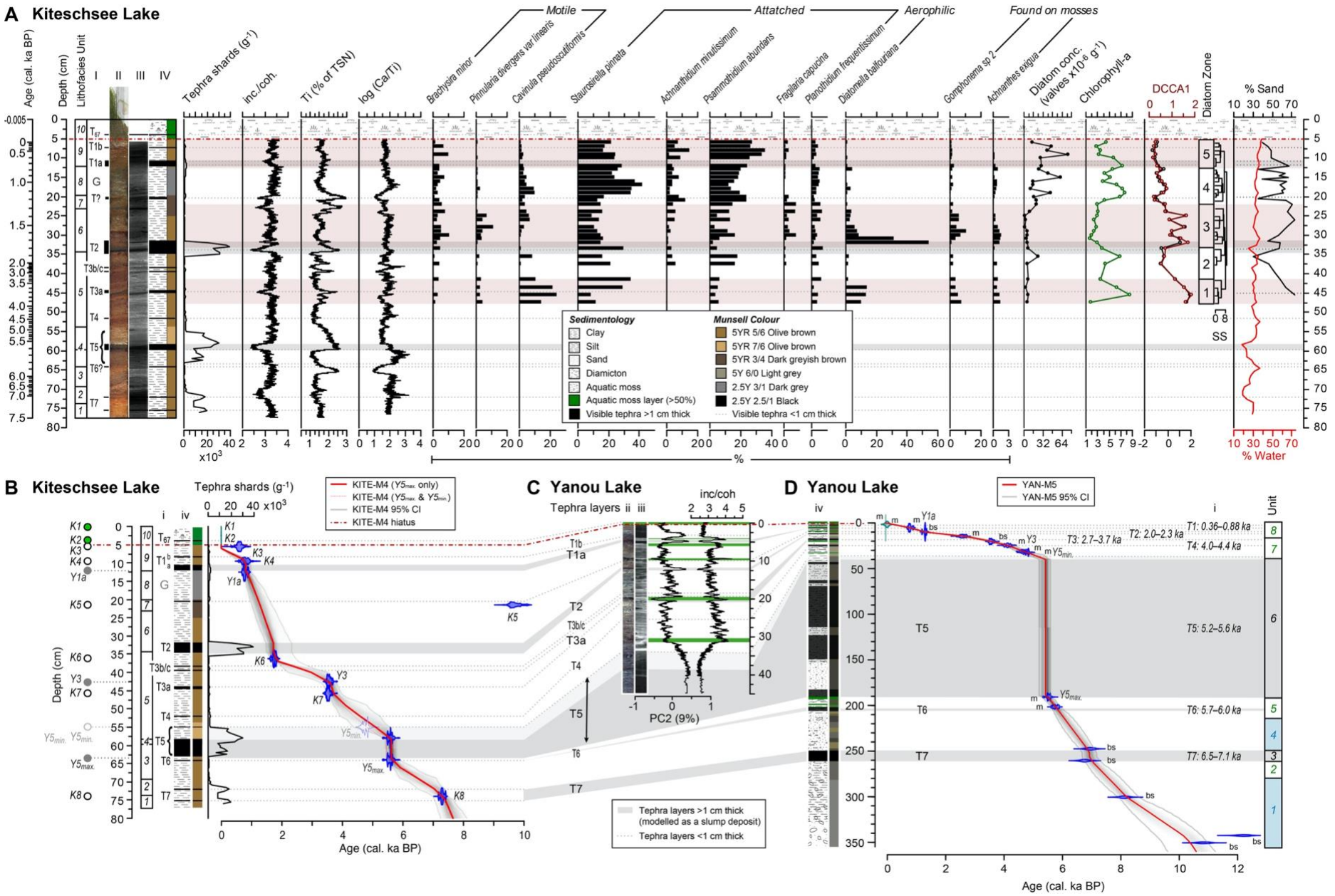
A Kiteschsee Lake
Motile
Attatched
Aerophilic
Found on mosses
Brachysira minor
Pinnularia divergens var linearis
Cavinula pseudoscutiformis
Staurosirella pinnata
Achnanthidium minutissimum
Psammothidium abundans
Fragilaria capucina
Planothidium frequentissimum
Diatoderella haffiuriana
Gomphonema sp 2
Achnanthes exigua
Tephra shards (g-1)
inc./coh.
Ti (% of TSN)
log (Ca/Ti)
Diatom conc. (valves x10-6 g-1)
Chlorophyll-a
DCCA1
Diatom Zone
% Sand
% Water
Sedimentology
Clay
Silt
Sand
Diamicton
Aquatic moss
Aquatic moss layer (>50%)
Visible tephra >1 cm thick
Munsell Colour
5YR 5/6 Olive brown
5YR 7/6 Olive brown
5YR 3/4 Dark greyish brown
5Y 6/0 Light grey
2.5Y 3/1 Dark grey
2.5Y 2.5/1 Black
Visible tephra <1 cm thick
B Kiteschsee Lake
KITE-M4 (Y5max. only)
KITE-M4 (Y5max. & Y5min.)
KITE-M4 95% CI
KITE-M4 hiatus
Age (cal. ka BP)
C Yanou Lake
Tephra layers
inc/coh
PC2 (9%)
Tephra layers >1 cm thick (modelled as a slump deposit)
Tephra layers <1 cm thick
D Yanou Lake
YAN-M5
YAN-M5 95% CI
T1: 0.36–0.88 ka
T2: 2.0–2.3 ka
T3: 2.7–3.7 ka
T4: 4.0–4.4 ka
T5: 5.2–5.6 ka
T6: 5.7–6.0 ka
T7: 6.5–7.1 ka
Unit

Figure 4. Summary of key stratigraphic, diatom and chronological data from the Kiteschsee Lake record; I = Tephra layers in the Kiteschsee Lake record, II = ITRAX XRF-CS optical image, III = ITRAX X-radiograph (positive image), IV = Summary lithology and RGB Munsell colour. B) Bayesian best fit age-depth model for the Kiteschsee Lake record. Sample thicknesses were 0.5 cm or 1 cm, and no zero-depth surface age was set in the age-depth model. Run settings and priors are shown in Figure S4. Modelled ages and errors were derived from the MCMC 'best-fit' weighted mean ages from the BACON age-depth model. Initial age model runs were fine-tuned by tephrastratigraphic correlation to the nearby Yanou Lake record and the inclusion of radiocarbon ages of subaquatic freshwater moss immediately below and above the 'T5', between the 'T3a' and 'T3b' tephra layers, and immediately below the 'T1a' layer in the Yanou Lake record (Supplementary Material for details). C) Age depth model and tephrastratigraphic correlation for the Yanou Lake record. D) An updated Bayesian age-depth model (2020 calibration) for the Yanou Lake record (cf. Roberts et al. 2017). All measured radiocarbon ages were included in age-depth models.

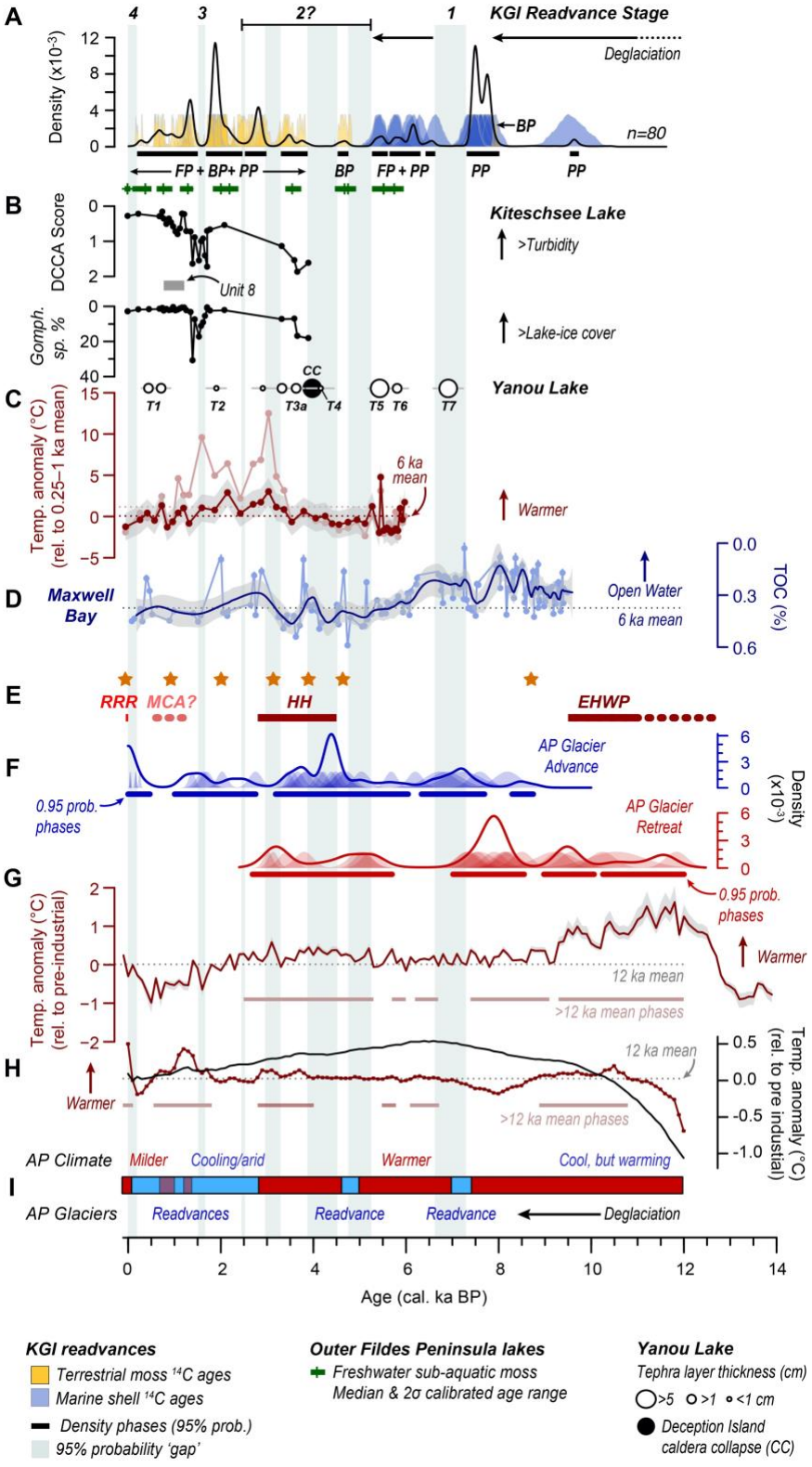

Figure 5. Regional palaeoclimatic context for Holocene glacier fluctuations on the South Shetland Islands, Antarctic Peninsula. A) Probability density phase model for glacier readvances Stages 1–4 on King George Island between 12–0 cal. ka BP and outer Fildes Peninsula freshwater subaquatic moss layers (median age and two-sigma age range) (Figure

3D-E for details); BP=Barton Peninsula; FP=Fildes Peninsula, PP=Potter Peninsula; units for the probability density phase analysis are cal. ka BP^{-1}. B) Diatom-inferred reconstructions and key indicator diatom species for Kiteschsee Lake. Lower DCCA scores reflect more turbid conditions, and lower *Gomphonema* sp. percentages represent less aerophilic conditions, and longer seasonal ice-cover. C) Glycerol dialkyl glycerol tetraether (GDGT) mean summer air temperature (MSAT) anomaly reconstruction and tephra layers from the Yanou Lake record (Foster et al., 2016; Roberts et al., 2017; Supplementary Materials for details). The dark red plot and its 6 ka mean (0.06±1.50 °C: dark red dotted line) are a new MSAT anomaly reconstruction (relative to the 250–1000 cal. a BP mean (±SD) value of 1.74±1.44 °C) for Yanou Lake, with RMSE of 1.65 °C shaded in grey (updated 2020 age calibration). This reconstruction is more realistic than the light red plot and its 6 ka mean (1.17±3.46 °C: light red dotted line) in Roberts et al. (2017). Airfall tephra layer ages are plotted above as modelled mean ages (white circles) and 95% confidence intervals (grey bars) and classified according to layer thickness in the Yanou Lake record. The timing of the caldera collapse (CC) eruption event from Antoniades et al. (2018) is also shown (black circle – mean age with two-sigma error within). The age-depth models in Roberts et al. (2017) and the caldera collapse eruption event age in Antoniades et al. (2018) have been updated to 2020 calibrations; Table S1B; Supplementary Materials for details). D) Maxwell Bay total organic carbon (%TOC) record (see Figure 6 for location) with lower values interpreted by Milliken et al. (2009) as reduced sea-ice concentration and more open water; the light blue plot is the published data; the dark blue line is a 100-yr interval LOESS regression with standard errors shaded in grey (LOESS = locally weighted sum of squares with tricube weighting and polynomial regression applied to the published %TOC data). E) Holocene warm periods on the Antarctic Peninsula (red bars; EHWP = Early Holocene Warm Period; HH = Holocene Hypsithermal; MCA = Medieval Climate Anomaly; RRR = Recent Rapid Regional warming; Bentley et al., 2009) and peaks greater than the 10 ka mean in the Total Solar Irradiance deviation (ΔTSI) (orange stars; see Figure 7A for explanation). F) Probability density phase model for glacier advance (blue) and retreat (red) data on the northern Antarctic Peninsula in Kaplan et al. (2020); units for the probability density phase analysis are cal. ka BP^{-1}. G) Temperature anomaly relative to pre-industrial reference period (1850–1900 CE) from the James Ross Island (JRI) ice core record, NE Antarctic Peninsula (Mulvaney et al., 2012); grey shading represents the published error range; the dotted line is the 12 ka mean. H) Holocene palaeotemperature compilation showing the median temperature anomaly for the 60–90 °S data stack (dark red line) and the temperature anomaly for the global data stack (black line) relative to the 'pre-industrial' reference period

(1850–1900 CE) (Kaufman et al., 2020a, b). The grey dotted line is the average median 12 ka temperature anomaly value of 0.02±0.14 °C for the 60–90 °S dataset; 95% CI errors in both datasets are, on average, +1.51 °C and -2.20 °C, mostly out of range and not plotted for clarity. I) Climate syntheses for the Antarctic Peninsula (Ingólfsson et al., 2003; Bentley et al., 2009).

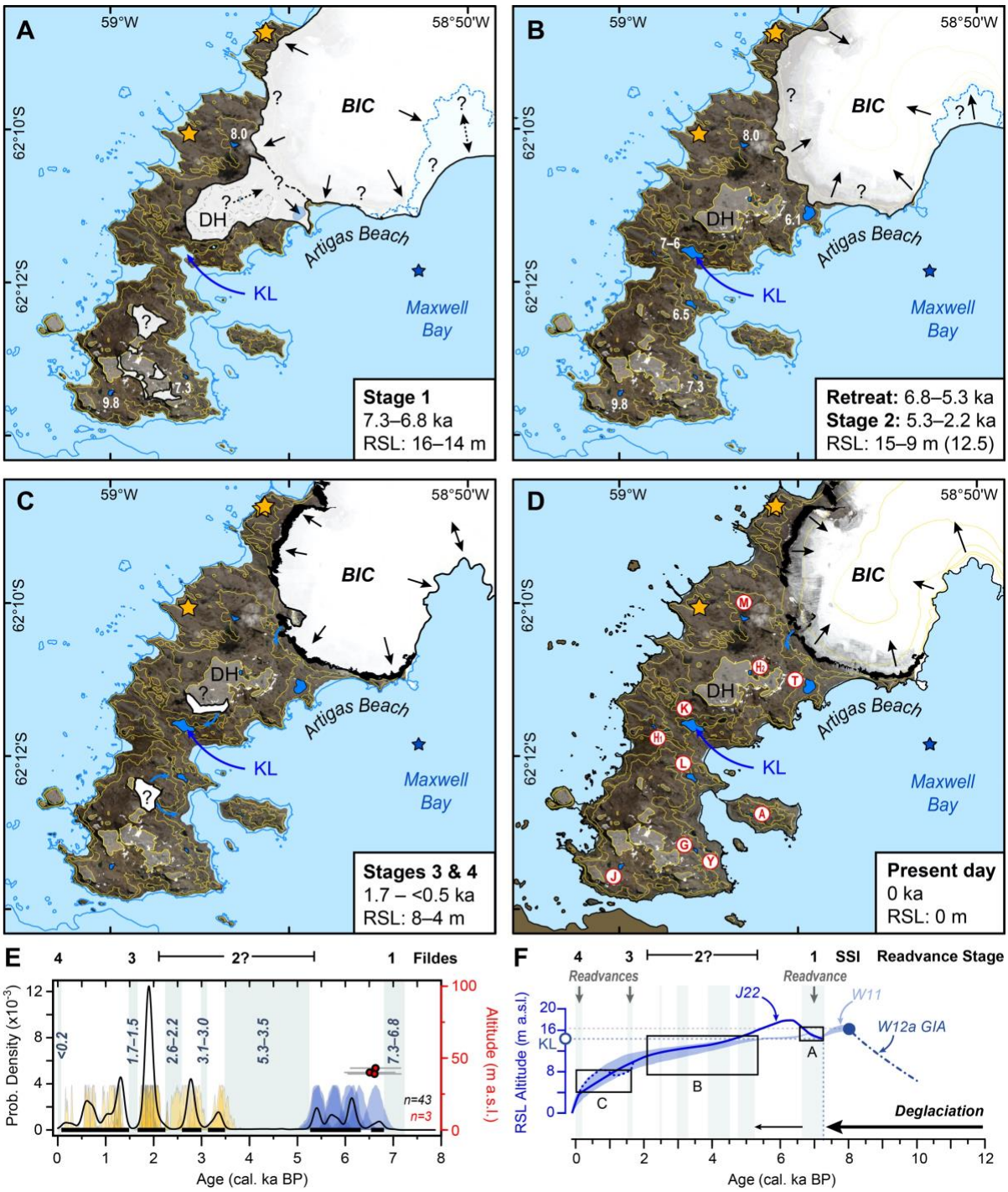

Figure 6. A–D) Schematic reconstruction of Mid- to Late Holocene glacier readvance extents during Stages 1–4 on the Fildes Peninsula. Glacier extents shown in A–C are based on a

compilation of new and published chronological data (panel E) for the Shetland I moraine (dark shading in C and D). E) Radiocarbon ages and probability density phase model for age constraints on glacier readvance on the Fildes Peninsula (n=43; Figure 3C for details; yellow distributions are radiocarbon ages of terrestrial material embedded in moraines; blue distributions are radiocarbon ages of marine material embedded in moraines; red circles with grey external error bars are ^{10}Be cosmogenic nuclide exposure ages obtained from boulders (orange stars in A–D); units for the probability density phase analysis are cal. ka BP^{-1}. F) Summarised relative sea level (RSL) curves for the South Shetland Islands (Watcham et al., 2011 – W11; Whitehouse et al., 2012a, b – W12aGIA; Johnson et al., 2022 – J22) used to determine the elevation of the coastlines in panels A–C; BIC = Bellingshausen Ice Cap; DH = Davies Heights; KL = Kiteschsee Lake, which is a marine embayment in A; the blue star is the location of Maxwell Bay marine records referred to in the text (Milliken et al., 2009; Simms et al., 2011); white areas (90% transparency) bordered by solid black lines in A–C are schematic representations of BIC extent on the Fildes Peninsula for each stage; present-day moraines mapped in this study are shown in D; black arrows represent schematic glacier flow directions, except in B where they represent retreat close to (or within) present day limits between 6.8–5.3 ka BP, followed by minor readvances close to present limits between 5.3–2.2 ka BP; blue arrows are main meltwater pathways. Question marks in A and B indicate tentative locations of potential glacier fronts above 100 m a.s.l.; lakes sediment basal and/or freshwater transition ages shown as white text are in cal. ka BP, labelled as in Figure 1. Black shaded areas around the BIC in C and D are the last readvance moraines, as shown in Figure 2. The 2013 CE satellite image of the BIC is shown in D, with studied lakes in blue (labelled as in Figure 1: white circles/red borders). Yellow lines are contours at 20 m, 40 m and 100 m elevation, with areas >100 m shaded white (30% transparency). The VHR satellite image in A–D is from Maxar Products: WorldView-2 image acquired 11th April 2013 © 2021 Maxar Technologies. This figure includes material copyright of Maxar Technologies, All Rights Reserved, reproduced here at low resolution with permission under a NERC-BAS educational licence and not included as part of a Creative Commons licence.

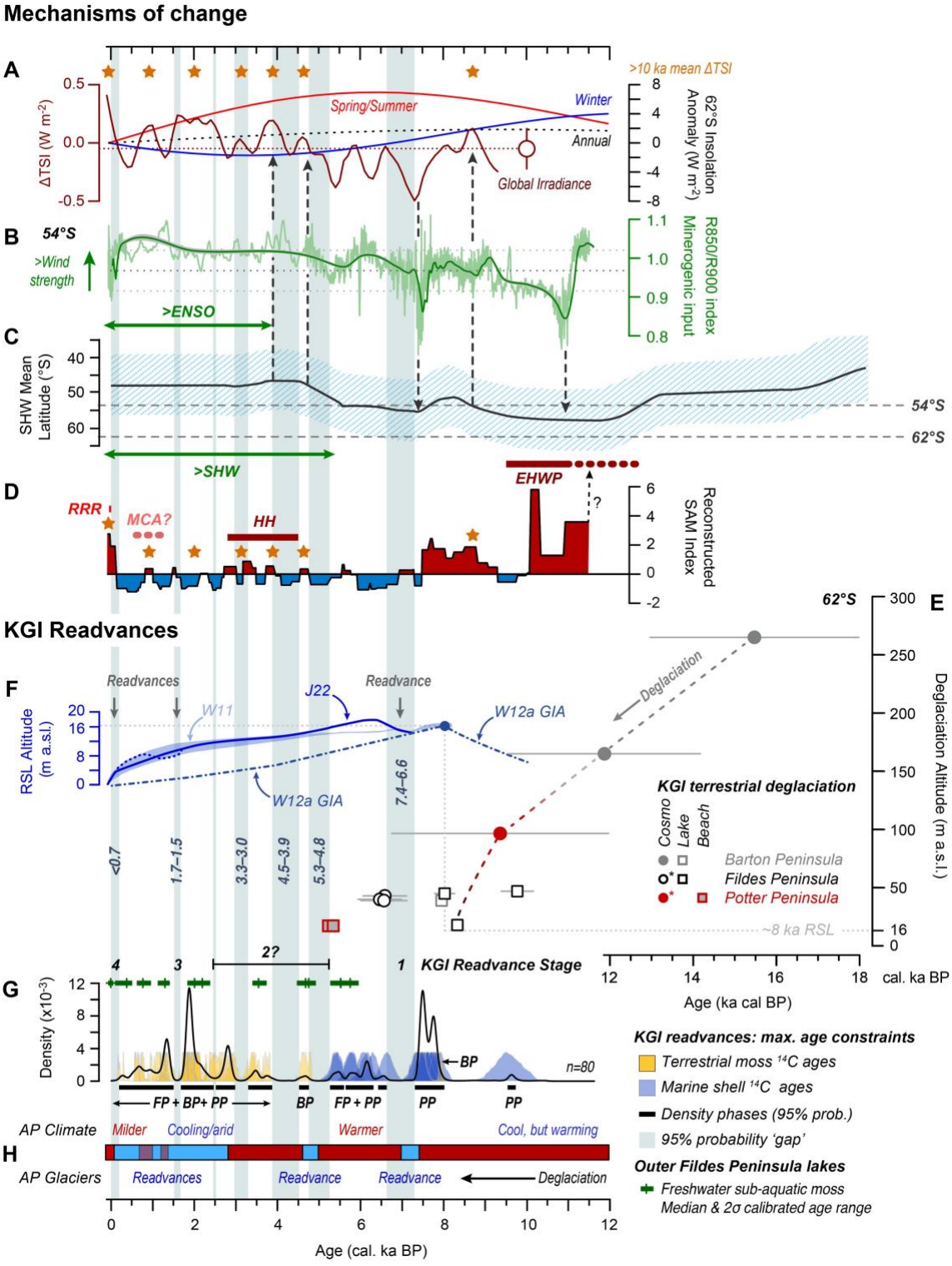

Figure 7 Mechanisms of deglaciation and glacier fluctuations on the Fildes Peninsula and King George Island (KGI). A) Total Solar Irradiance, which is the power per unit area received from the Sun as measured, or reconstructed, on Earth, where ΔTSI represents the deviation from its present-day value (Steinhilber et al., 2009) compared with solar insolation received at 62°S during the Holocene (11.75 ka) (Laskar et al., 2004); annual insolation = dotted black line,

austral spring/summer (SONDJF) insolation = red line; winter (JJA) insolation = blue line; the open dark red circle is the mean±1σ ΔTSI value for the last 10 ka; orange stars mark ΔTSI peaks greater than the 10 ka mean value. B) Ultra-high resolution (69 μm) hyperspectral (SPECIM) R850/R900 data, a proxy for mineral input into the Emerald Lake, Macquarie Island at 54°S (Saunders et al., 2018; age model updated to Sh20.cal), which reflects changes Southern Hemisphere Westerly wind (SHW) strength during the mid–late Holocene; the dark grey horizontal dotted line is the R850/R900 dataset mean; dark green line is 100-year interval LOESS smoothing of the R850/R900 (see code for details). C) Hypothetical representation of changes in the mean annual latitudinal position of the core SHW intensity belt (dark grey line) and approximate 1σ latitudinal range of enhanced precipitation (light blue stipple) (Ariztegui et al., 2010; Quade and Kaplan, 2017). In reality, the SHW are more intense and focused during positive (warmer) phases of the SAM, but weaker, latitudinally broader and less focused during negative (colder) phases of the SAM, show in D. The light grey horizontal dashes are 54°S (Macquarie Island) and 62°S (South Shetland Islands); vertical dashed lines and arrows highlight the key hypothesised latitudinal shifts of the Holocene and their relationship to the global irradiance profile shown in A; ENSO = El Niño Southern Oscillation. D) Reconstructed Holocene SAM-index variability between positive (red) to negative (blue) SAM-like conditions based on Northern Arboreal Pollen data from Southern Chile (Moreno et al., 2018) compared with ΔTSI >10 ka mean peaks (orange stars), and warm periods on the Antarctic Peninsula (EHWP = Early Holocene Warm Period; HH = Holocene Hypsithermal; MCA = Medieval Climate Anomaly; RRR = Recent Rapid Regional warming; Bentley et al., 2009). E) Summarised relative sea level (RSL) envelope for the SSI (W11; light blue shading; Watcham et al., 2011) compared with the RSL curve in Johnson et al. (2022) (J22; dark solid and dotted blue lines) and the W12a GIA model (Whitehouse et al., 2012a, b); see original references for data and further details. F) Cosmogenic nuclide exposure ages and key lake basal age constraints on deglaciation for terrestrial ice-free peninsulas on KGI at different altitudes from the Fildes Peninsula (this study), the Potter Peninsula (Heredia Barión et al., 2023), and the Barton Peninsula (Seong et al., 2008; Oliva et al., 2019) (secondary plot); * = new data (this study). G) Probability density phase model for glacier readvances Stages 1–4 on King George Island between 12–0 cal. ka BP (Figure 3D for details); BP=Barton Peninsula; FP=Fildes Peninsula, PP=Potter Peninsula; units for the probability density phase analysis are cal. ka BP^{-1}. H) Glacier-climate syntheses for the Antarctic Peninsula (adapted from Ingólfsson et al. (2003) and Bentley et al. (2009)).

Sample ID	AMS ID	Latitude (°S) Longitude (°W)	Altitude (m a.s.l.)	Boulder dimension (L x W x H) (m)	Sample thickness (cm)	^{10}Be concentration (atoms g^{-1})	^{10}Be concentration 1σ (atoms g^{-1})	^{10}Be age (yr) (Ww) ± 1σ int (ext) error	^{10}Be age (yr) (Pt) ± 1σ ext. error	^{10}Be age (yr) (Kp) ± 1σ ext. error	Context
Fildes1	s08808	62° 10' 2.34" S 58° 57' 45.97" W	43	2.65 x 2.10 x 1.98	1.4	37.1 x 10^3	1.9 x 10^3	6630 ± 340 (520)	6640 ± 350	6830 ± 660	Erratic (retreat)
Fildes2	s08809	62° 08' 43.65" S 58° 55' 35.96" W	40	0.87 x 0.71 x 0.35	1.2	36.4 x 10^3	2.0 x 10^3	6510 ± 350 (520)	6530 ± 370	6710 ± 660	Erratic (retreat)
Fildes3	s08810	62° 08' 43.97" S 58° 55' 37.18" W	39	0.74 x 0.62 x 0.26	1.2	36.9 x 10^3	2.2 x 10^3	6610 ± 390 (550)	6630 ± 400	6810 ± 680	Erratic (retreat)

Table 1. Cosmogenic surface exposure dating results. Exposure ages were calculated using version 3 of the online calculator described by Balco et al., (2008). Following standard procedures for the Antarctic Peninsula region, we used the Antarctic ("Ant") pressure flag and the scaling scheme "LSDn" (Stone, 2000; Lifton et al., 2014). We employed the scaling model "LSDn" because it derives from an improved understanding of the atmospheric particle flux and neutron spectrum (Lifton et al., 2014), as compared with other scaling schemes using empirical fits to proxy data. A rock density of 2.7 g cm^{-3} was assumed for the samples. Exposure ages are derived using the default ^{10}Be production rate calibration dataset (Borchers et al., 2016) in the v. 3 of the online calculator of Balco et al (2008). However, for comparison, ^{10}Be ages were calculated using the mid-latitude southern hemisphere New Zealand (Putnam et al., 2010) and Patagonian calibration datasets (Kaplan et al., 2011) since these are proximal to Antarctica. No snow cover or erosion rate correction was applied. Internal and external uncertainties (Balco et al., 2008) are reported and we use external uncertainties to compare new exposure ages with calibrated AMS radiocarbon ages collected in this study. In the online calculator, we assumed zero erosion, used the AMS standard flag 07KNSTD, an "ant" elevation pressure flag and a density of 2.7 g cm^{-2}. A shielding correction of 0.9999 was applied to all samples as the value is the same for all. Calculations of ^{10}Be exposure ages using the global (Ww) "LSDn" scaling (Lifton et al., 2014), the New Zealand-Macaulay (Pt) (Putnam et al., 2010), and the Patagonia calibration dataset (Kp) (Kaplan et al., 2011) are shown. int: Internal error; ext: External error; ages have been rounded to the nearest 10 years. Lm production rate scaling from the online calculator (Balco et al., 2008) would give ages that are around 2% older, within the uncertainties on the ages we report using LSDn. For the batch of three

samples, the laboratory blank used to correct ^{10}Be concentrations was 2.06 x10^{-15} ± 3.71x10^{-16}, amounting to a maximum background correction of less than 6% of the total ^{10}Be atoms measured.

ID No.	Location Sample ID]	Lab. ID	Latitude (°S)	Longitude (°W)	Alt. (m a.s.l.)	Material dated	δ^{13}C (‰)	AMS ^{14}C age (^{14}C a)	Calibrated ages (cal. a BP)					
									Max.–Min.	1σ %	Max.–Min.	2σ %	Median	Mean ± 2σ
1	ART-03A-2015	Beta-441409	62° 10' 46.20"	58° 53' 58.34"	72	Terrestrial moss	-22.7	1380 ± 30	1300–1260	37.9	1310–1170	95.4	1250	1240 ± 80
									1210–1180	30.4	–	–		
2	ART-03B-2015	Beta-441410	62° 10' 46.20"	58° 53' 58.34"	72	Terrestrial moss	-20.5	1380 ± 30	1300–1260	37.9	1310–1170	95.4	1250	1240 ± 80
									1210–1180	–	–			
3	ART-01A-2015	Beta-441405	62° 10' 46.20"	58° 53' 58.34"	72	Terrestrial moss	-22.6	1980 ± 30	1890–1820	62.6	1930–1740	95.4	1850	1850 ± 100
									1770–1750	5.7	–	–		
4	ART-01B-2015	Beta-441406	62° 10' 46.20"	58° 53' 58.34"	72	Terrestrial moss	-22.4	1950 ± 30	1870–1850	14.8	1890–1730	95.4	1810	1810 ± 100
									1840–1740	53.5	–	–		
5	ART-01A-2015 bis	Beta-441407	62° 10' 46.20"	58° 53' 58.34"	72	Terrestrial moss	-19.6	1920 ± 30	1890–1820	58.0	1930–1740	95.4	1840	1830 ± 100
									1770–1750	10.3	–	–		
6	ART-01B-2015 bis	Beta-441408	62° 10' 46.20"	58° 53' 58.34"	72	Terrestrial moss	-16.8	1940 ± 30	2000–1920	60.0	2010–1870	95.4	1950	1940 ± 80
									1910–1890	8.2	–	–		
7	ART-08-ar-A-2015	Beta-441411	62° 10' 54.52"	58° 51' 43.94"	16	Terrestrial moss	-17.9	2030 ± 30	2010–1920	68.3	2050–2030	1.8	1960	1960 ± 80
									–	–	2020–1880	93.6		
8	ART-08-ar-B-2015	Beta-441412	62° 10' 54.52"	58° 51' 43.94"	16	Terrestrial moss	-24.5	2050 ± 30	1820–1720	68.3	1840–1690	94.4	1770	1760 ± 80
									–	–	1650–1630	1.0		
9	ART-08-ab-A-2015	Beta-441413	62° 10' 54.52"	58° 51' 43.94"	16	Terrestrial moss	-20.9	1870 ± 30	1830–1740	68.3	1880–1700	95.4	1790	1790 ± 80

10	ART-08-ab-B-2015	Beta-441414	62° 10' 54.52"	58° 51' 43.94"	16	Terrestrial moss	-28.6	1900 ± 30	2010–1920	68.3	2050–2030	1.8	1960	1960 ± 80
									–	–	2020–1880	93.6		
11	ART-02-1A	Beta-441415	62° 10' 56.07"	58° 53' 22.15"	7	Terrestrial moss	-20.5	2050 ± 30	2000–1960	24.0	2000–1830	95.4	1920	1930 ± 80
									1940–1880	44.2	–	–		
12	ART-02-2A	Beta-441417	62° 10' 56.07"	58° 53' 22.15"	7	Terrestrial moss	-21.9	2010 ± 30	1930–1830	68.3	2000–1950	12.6	1890	1890 ± 100
									–	–	1940–1820	81.6		
									–	–	1770–1750	1.3		
13	ART-02-2B	Beta-441418	62° 10' 56.07"	58° 53' 22.15"	7	Terrestrial moss	-23.7	1980 ± 30	1930–1830	68.3	2000–1750	95.4	1890	1890 ± 100
14	ART-07A-2015	ETH-69688	62° 10' 51.73"	58° 51' 39.45"	18	*Laternula* sp.shell	-0.9	7045 ± 85	6790–6480	68.3	6940–6330	95.4	6630	6640 ± 300
15	ART-07B-2015	ETH-69689	62° 10' 51.73"	58° 51' 39.45"	18	*Laternula* sp.shell	4.0	6590 ± 70	6270–6000	68.3	6400–5880	95.4	6140	6140 ± 260
16	ART-07C-2015	ETH-69690	62° 10' 51.73"	58° 51' 39.45"	18	*Laternula* sp.shell	0.0	6730 ± 75	6440–6160	68.3	6570–6000	95.4	6300	6290 ± 280
17	ART-09A-2015	ETH-69691	62° 10' 50.59"	58° 51' 40.66"	27	*Laternula* sp.shell	-2.2	6265 ± 75	5920–5640	68.3	6090–5530	95.4	5790	5790 ± 280
18	ART-09B-2015	ETH-69692	62° 10' 50.59"	58° 51' 40.66"	27	*Laternula* sp.shell	3.4	5895 ± 70	5550–5280	68.3	5660–5080	95.4	5400	5390 ± 280
19	ART-10A-2015	ETH-69693	62° 10' 49.04"	58° 51' 34.88"	28	*Laternula* sp.shell	0.9	6235 ± 70	5890–5620	68.3	6020–5480	95.4	5760	5760 ± 260
20	ART-10B-2015	ETH-69694	62° 10' 49.04"	58° 51' 34.88"	28	*Laternula* sp.shell	-1.2	5925 ± 70	5560–5300	68.3	5700–5130	95.4	5430	5420 ± 260
21	ART-10C-2015	ETH-69695	62° 10' 49.04"	58° 51' 34.88"	28	*Laternula* sp.shell	-2.8	6520 ± 75	6200–5930	68.3	6330–5780	95.4	6070	6070 ± 260
22	ART-04A-2015	ETH-69684	62° 10' 23.69"	58° 54' 59.09"	42	*Laternula* sp.shell	-1.4	>44300 ± 4430	45510–45040	68.3	45730–44830	95.4	45280	45280 ± 460
23	ART-04B-2015	ETH-69685	62° 10' 23.69"	58° 54' 59.09"	42	*Laternula* sp.shell	2.8	>43700 ± 4370	44970–44580	68.3	45210–44430	95.4	44790	44800 ± 400
24	ART-05A-2015	ETH-69686	62° 10' 24.55"	58° 54' 59.05"	42	*Laternula* sp.shell	2.8	>48500 ± 4850	50090–49170	68.3	50800–48710	95.4	49690	49720 ± 1120

25	ART-05B-2015	ETH-69687	62° 10' 24.55"	58° 54' 59.05"	42	*Laternula* sp.shell	-	>51700 ± 5170	51900–51490	68.3	52120–51300	95.4	51700	51700 ± 400
26	K1-M [0–0.5 cm]	Beta-501582	62° 11' 36.55"	58° 57' 59.93"	15	*Drepanocladus l.* sp.	-27.4	-100 ± 30	-6 – -7	68.3	-5 – -7	95.4	-6	-6 ± 1
27	K2-M [4.5-5 cm]	Beta-516809	62° 11' 36.55"	58° 57' 59.93"	15	*Drepanocladus l.* sp.	-29.3	-130 ± 30	-6 – -7	68.3	-6 – -7	95.4	-7	-7 ± 1
28	K3-BS [5-6 cm]*	Beta-516810	62° 11' 36.55"	58° 57' 59.93"	15	Bulk sediment	-18.4	1350 ± 30*	650–460	68.3	750–370	95.4	560	560 ± 180
29	K4-BS [9–10 cm]*	Beta-504801	62° 11' 36.55"	58° 57' 59.93"	15	Bulk sediment	-23.9	1600 ± 30*	910–700	68.3	1010–600	95.4	800	800 ± 200
30	K5-BS [20–21 cm]*	Beta-497408	62° 11' 36.55"	58° 57' 59.93"	15	Bulk sediment	-32.6	9380 ± 30*	10030–9790	68.3	10130–9660	95.4	9910	9900 ± 240
31	K6-BS [36.5–37 cm]	Beta-501584	62° 11' 36.55"	58° 57' 59.93"	15	Bulk sediment	-18.0	1860 ± 30	1820–1770	27.8	1830–1690	90.6	1750	1750 ± 100
									1750–1700	40.5	1650–1620	4.9		
32	K7-BS [45.5–46 cm]	Beta-501585	62° 11' 36.55"	58° 57' 59.93"	15	Bulk sediment	-17.7	3350 ± 30	3570–3480	68.3	3680–3670	1.0	3530	3530 ± 100
									–	–	3640–3450	94.5		
33	K8-BS [73.5–74.5 cm]	Beta-498331	62° 11' 36.55"	58° 57' 59.93"	15	Bulk sediment	-18.0	6410 ± 30	7420–7390	9.1	7430–7240	85.5	7300	7300 ± 120
									7330–7250	29.2	7210–7170	10.0		

Table 2. New radiocarbon age data from the eastern Shetland I Moraine and the Kiteschsee Lake record on the Fildes Peninsula (see text and Supplementary Materials for further details). Dating replicates were used to assess dating and interpretation accuracy. Elevation data (Alt. m a.s.l. – Altitude in metres above present sea level) were taken with a Garmin handheld GPS map 62stc, precision ±2 m (latitude, longitude) and altitudinal precision of ±5–10 m. Calibrated and modelled radiocarbon ages have been rounded to the nearest 10 years, with two-sigma calibrated ages or 95% confidence age-depth model age ranges quoted in the text. A 700±100 ^{14}C year lake reservoir effect was applied to bulk sediment radiocarbon ages from units 7-9 in Kiteschsee Lake indicated by asterisks, based on the average age offset between ages for the T1 tephra layer in Kiteschsee Lake and Yanou Lake (Supplementary Materials for details).

References

Antoniades D, Giralt S, Geyer A, Álvarez-Valero AM, Pla-Rabes S, Granados I, et al. (2018) The timing and widespread effects of the largest Holocene volcanic eruption in Antarctica. *Scientific Reports* 8: 17279.

Ariztegui D, Gilli A, Anselmetti FS, Goñi RA, Belardi JB and Espinosa S. (2010) Lake-level changes in central Patagonia (Argentina): crossing environmental thresholds for Lateglacial and Holocene human occupation. *Journal of Quaternary Science* 25: 1092-1099.

Baggenstos D, Häberli M, Schmitt J, Shackleton SA, Birner B, Severinghaus JP, et al. (2019) Earth's radiative imbalance from the Last Glacial Maximum to the present. *Proceedings of the National Academy of Sciences* 116: 14881-14886.

Balco G. (2011) Contributions and unrealized potential contributions of cosmogenic-nuclide exposure dating to glacier chronology, 1990–2010. *Quaternary Science Reviews* 30: 3-27.

Balco G and Schaefer JM. (2013) Exposure-age record of Holocene ice sheet and ice shelf change in the northeast Antarctic Peninsula. *Quaternary Science Reviews* 59: 101-111.

Balco G, Stone JO, Lifton NA and Dunai TJ. (2008) A complete and easily accessible means of calculating surface exposure ages or erosion rates from 10Be and 26Al measurements. *Quaternary Geochronology* 3: 174-195.

Bañón M, Justel A, Velázquez D and Quesada A. (2013) Regional weather survey on Byers Peninsula, Livingston Island, South Shetland Islands, Antarctica. *Antarctic Science* 25: 146-156.

Barsch D and Mäusbacher R. (1986) New Data on the Relief Development of the South Shetland Islands, Antarctica. *Interdisciplinary Science Reviews* 11: 211-218.

Bentley MJ, Hodgson DA, Smith JA and Cox NJ. (2005) Relative sea level curves for the South Shetland Islands and Marguerite Bay, Antarctic Peninsula. Quaternary Science Reviews 24: 1203-1216.

Bentley MJ, Evans DJA, Fogwill CJ, Hansom JD, Sugden DE and Kubik PW. (2007) Glacial geomorphology and chronology of deglaciation, South Georgia, sub-Antarctic. *Quaternary Science Reviews* 26: 644-677.

Bentley MJ, Hodgson DA, Smith JA, Cofaigh CÓ, Domack EW, Larter RD, et al. (2009) Mechanisms of Holocene palaeoenvironmental change in the Antarctic Peninsula region. *The Holocene* 19: 51-69.

Birkenmajer, K. (1989). A guide to Tertiary geochronology of King George Island, West Antarctica. *Polish Polar Research* 10: 555-579.

Bevan A. (2021) Rcarbon: Calibration and Analysis of Radiocarbon Dates. *https://github.com/ahb108/rcarbon/*.

Binnie SA, Dunai TJ, Voronina E, Goral T, Heinze S and Dewald A. (2015) Separation of Be and Al for AMS using single-step column chromatography. *Nuclear Instruments and Methods in Physics Research Section B: Beam Interactions with Materials and Atoms* 361: 397-401.

Björck S, Hjort, C., Ingolfsson, O., Skog, G. (1991a) Radiocarbon dates from the Antarctic Peninsula region — problems and potential. In: Lowe JJ (ed) *Radiocarbon dating: recent applications and future potential.* Quaternary Proceedings 1: 55–65.

Björck S, Nils Malmer, Christian Hjort, Per Sandgren, Ólafur Ingólfsson, Bo Wallén, Ronald Ian Lewis Smith, and Bodil Liedberg Jónsson. (1991b) Stratigraphic and Paleoclimatic Studies of a 5500-Year-Old Moss Bank on Elephant Island, Antarctica. *Arctic and Alpine Research* 23: 361-374.

Björck S, Håkansson H, Olsson S, Barnekow L and Janssens J. (1993) Palaeoclimatic studies in South Shetland Islands, Antarctica, based on numerous stratigraphic variables in lake sediments. *Journal of Paleolimnology* 8: 233-272.

Blaauw M and Christen JA. (2011) Flexible paleoclimate age-depth models using an autoregressive gamma process. *Bayesian Analysis* 6: 457-474.

Blockley SPE, Pyne-O'Donnell SDF, Lowe JJ, Matthews IP, Stone A, Pollard AM, et al. (2005) A new and less destructive laboratory procedure for the physical separation of distal glass tephra shards from sediments. *Quaternary Science Reviews* 24: 1952-1960.

Borchers B, Marrero S, Balco G, Caffee M, Goehring B, Lifton N, et al. (2016) Geological calibration of spallation production rates in the CRONUS-Earth project. *Quaternary Geochronology* 31: 188-198.

Braun M, Saurer H, Gossmann H. (2004) Climate, energy fluxes and ablation rates on the ice cap of King George Island. *Pesquisa Antártica Brasileira* 4: 87– 103.

Bronk Ramsey C. (2009) Bayesian Analysis of Radiocarbon Dates. *Radiocarbon* 51: 337-360.

Bulínová, M., Kohler, T.J., Kavan, J., Van De Vijver, B., Nývlt, D., Nedbalová, L., Coria, S.H., Lirio, J.M., and Kopalová, K. (2020). Comparison of Diatom Paleo-Assemblages with Adjacent Limno-Terrestrial Communities on Vega Island, Antarctic Peninsula. Water 12, 1340.

Čejka T, Nývlt D, Kopalová K, Bulínová M, Kavan J, Lirio JM, et al. (2020) Timing of the neoglacial onset on the North-Eastern Antarctic Peninsula based on lacustrine archive from Lake Anónima, Vega Island. *Global and Planetary Change* 184: 103050.

Charman DJ, Amesbury MJ, Roland TP, Royles J, Hodgson DA, Convey P, et al. (2018) Spatially coherent late Holocene Antarctic Peninsula surface air temperature variability. *Geology* 46: 1071-1074.

Christeson GL, Barker DHN, Austin Jr. JA and Dalziel IWD. (2003) Deep crustal structure of Bransfield Strait: Initiation of a back arc basin by rift reactivation and propagation. *Journal of Geophysical Research: Solid Earth* 108.

Chu Z, Sun L, Wang Y, Huang T and Zhou X. (2017) Depositional environment and climate changes during the Holocene in Grande Valley, Fildes Peninsula, King George Island, Antarctica. *Antarctic Science* 29: 545-554.

Davies BJ, Glasser NF, Carrivick JL, Hambrey MJ, Smellie JL and Nývlt D. (2013) Landscape evolution and ice-sheet behaviour in a semi-arid polar environment: James Ross Island, NE Antarctic Peninsula. *Geological Society, London, Special Publications* 381: 353-395.

Davies BJ, Golledge NR, Glasser NF, Carrivick JL, Ligtenberg SRM, Barrand NE, et al. (2014) Modelled glacier response to centennial temperature and precipitation trends on the Antarctic Peninsula. *Nature Climate Change* 4: 993-998.

Davies SJ, Lamb HF and Roberts SJ. (2015) Micro-XRF Core Scanning in Palaeolimnology: Recent Developments. In: Croudace IW and Rothwell RG (eds) *Micro-XRF Studies of Sediment Cores: Applications of a non-destructive tool for the environmental sciences.* Dordrecht: Springer Netherlands, 189-226.

de Pablo MA, Blanco JJ, Molina A, Ramos M, Quesada A and Vieira G. (2013) Interannual active layer variability at the Limnopolar Lake CALM site on Byers Peninsula, Livingston Island, Antarctica. *Antarctic Science* 25: 167-180.

Emslie SD, Romero M, Juáres MA and Argota MR. (2019) Holocene occupation history of pygoscelid penguins at Stranger Point, King George (25 de Mayo) Island, northern Antarctic Peninsula. *The Holocene*: 0959683619875814.

Etourneau J, Collins LG, Willmott V, Kim JH, Barbara L, Leventer A, et al. (2013) Holocene climate variations in the western Antarctic Peninsula: evidence for sea ice extent predominantly controlled by changes in insolation and ENSO variability. *Climate of the Past* 9: 1431-1446.

Falk U, López DA and Silva-Busso A. (2018) Multi-year analysis of distributed glacier mass balance modelling and equilibrium line altitude on King George Island, Antarctic Peninsula. *The Cryosphere* 12: 1211-1232.

Forte P and Castro JM. (2019) H2O-content and temperature limit the explosive potential of rhyolite magma during Plinian eruptions. *Earth and Planetary Science Letters* 506: 157-167.

Foster LC, Pearson EJ, Juggins S, Hodgson DA, Saunders KM, Verleyen E, et al. (2016) Development of a regional glycerol dialkyl glycerol tetraether (GDGT)–temperature calibration for Antarctic and sub-Antarctic lakes. *Earth and Planetary Science Letters* 433: 370-379.

Fretwell PT, Hodgson DA, Watcham EP, Bentley MJ and Roberts SJ. (2010) Holocene isostatic uplift of the South Shetland Islands, Antarctic Peninsula, modelled from raised beaches. *Quaternary Science Reviews* 29: 1880-1893.

Garreaud R. (2007) Precipitation and Circulation Covariability in the Extratropics. *Journal of Climate* 20: 4789-4797.

Geyer A, Álvarez-Valero AM, Gisbert G, Aulinas M, Hernández-Barreña D, Lobo A, et al. (2019) Deciphering the evolution of Deception Island's magmatic system. *Scientific Reports* 9: 373.

Glasser NF, Davies BJ, Carrivick JL, Rodés A, Hambrey MJ, Smellie JL, et al. (2014) Ice-stream initiation, duration and thinning on James Ross Island, northern Antarctic Peninsula. *Quaternary Science Reviews* 86: 78-88.

Goodwin BP, Mosley-Thompson E, Wilson AB, Porter SE and Sierra-Hernandez MR. (2016) Accumulation Variability in the Antarctic Peninsula: The Role of Large-Scale Atmospheric Oscillations and Their Interactions. *Journal of Climate* 29: 2579-2596.

Guglielmin M, Convey P, Malfasi F and Cannone N. (2016) Glacial fluctuations since the 'Medieval Warm Period' at Rothera Point (western Antarctic Peninsula). *The Holocene* 26: 154-158.

Gunn, D.E., and Best, A.I. (1998). A new automated nondestructive system for high resolution multi-sensor core logging of open sediment cores. *Geo-Marine Letters* 18**,** 70-77.

Hall, B.L. (2003). An Overview of Late Pleistocene Glaciation in the South Shetland Islands. In E. Domack, A. Levente, A. Burnet, et al. (eds) *Antarctic Peninsula Climate Variability: Historical and Paleoenvironmental Perspectives.* American Geophysical Union: 10.1029/AR079p0103

Hall BL. (2007) Late-Holocene advance of the Collins Ice Cap, King George Island, South Shetland Islands. *The Holocene* 17: 1253-1258.

Hall BL. (2009) Holocene glacial history of Antarctica and the sub-Antarctic islands. *Quaternary Science Reviews* 28: 2213-2230.

Hall BL. (2010) Holocene relative sea-level changes and ice fluctuations in the South Shetland Islands. *Global and Planetary Change* 74: 15-26.

Hall BL and Perry ER. (2004) Variations in ice rafted detritus on beaches in the South Shetland Islands: a possible climate proxy. *Antarctic Science* 16: 339-344.

Haslett J and Parnell A. (2008) A simple monotone process with application to radiocarbon-dated depth chronologies. *Journal of the Royal Statistical Society: Series C (Applied Statistics)* 57: 399-418.

Hass HC, Kuhn G, Monien P, Brumsack H-J and Forwick M. (2010) Climate fluctuations during the past two millennia as recorded in sediments from Maxwell Bay, South Shetland Islands, West Antarctica. *Geological Society, London, Special Publications* 344: 243-260.

Heaton TJ, Köhler P, Butzin M, Bard E, Reimer RW, Austin WEN, et al. (2020) Marine20—The Marine Radiocarbon Age Calibration Curve (0–55,000 cal BP). *Radiocarbon* 62: 779-820.

Heaton, T.J., Bard, E., Bronk Ramsey, C., Butzin, M., Hatté, C., Hughen, K.A., Köhler, P., and Reimer, P.J. (2022). A response to community questions on the Marine20 radiocarbon age calibration curve: marine reservoir ages and the calibration of ^{14}C samples from the oceans. *Radiocarbon*: 1-27. doi:10.1017/RDC.2022.66

Hein AS, Marrero SM, Woodward J, Dunning SA, Winter K, Westoby MJ, et al. (2016) Mid-Holocene pulse of thinning in the Weddell Sea sector of the West Antarctic ice sheet. *Nature Communications* 7: 12511.

Heredia Barión PA, Strelin JA, Roberts SJ, Spiegel C, Wacker L, Niedermann S, et al. (2023) The impact of Holocene deglaciation and glacial dynamics on the landscapes and geomorphology of Potter Peninsula, King George Island (Isla 25 Mayo), NW Antarctic Peninsula. *Frontiers in Earth Science* 10:1073075.

Hogg AG, Hua Q, Blackwell PG, Niu M, Buck CE, Guilderson TP, et al. (2013) SHCal13 Southern Hemisphere Calibration, 0–50,000 Years cal BP. *Radiocarbon* 55: 1889-1903.

Hogg AG, Heaton TJ, Hua Q, Palmer JG, Turney CSM, Southon J, et al. (2020) SHCal20 Southern Hemisphere Calibration, 0–55,000 Years cal BP. *Radiocarbon* 62: 759-778.

Hua Q, Barbetti M, and Rakowski AZ (2013). Atmospheric radiocarbon for the period 1950-2010. *Radiocarbon* 55, 1–14.

Ingólfsson Ó, Hjort C and Humlum O. (2003) Glacial and Climate History of the Antarctic Peninsula since the Last Glacial Maximum. *Arctic, Antarctic, and Alpine Research* 35: 175-186.

John BS and Sugden DE. (1971) Raised marine features and phases of glaciation in the South Shetland Islands. *British Antarctic Survey Bulletin* 24: 45-111.

Johnson JS, Bentley MJ, Roberts SJ, Binnie SA and Freeman SPHT. (2011) Holocene deglacial history of the northeast Antarctic Peninsula – A review and new chronological constraints. *Quaternary Science Reviews* 30: 3791-3802.

Johnson JS, Everest JD, Leat PT, Golledge NR, Rood DH and Stuart FM. (2012) The deglacial history of NW Alexander Island, Antarctica, from surface exposure dating. *Quaternary Research* 77: 273-280.

Johnson JS, Smith JA, Schaefer JM, Young NE, Goehring BM, Hillenbrand C-D, et al. (2017) The last glaciation of Bear Peninsula, central Amundsen Sea Embayment of Antarctica: Constraints on timing and duration revealed by in situ cosmogenic 14C and 10Be dating. *Quaternary Science Reviews* 178: 77-88.

Johnson JS, Roberts SJ, Rood DH, Pollard D, Schaefer JM, Whitehouse PL, et al. (2020) Deglaciation of Pope Glacier implies widespread early Holocene ice sheet thinning in the Amundsen Sea sector of Antarctica. *Earth and Planetary Science Letters* 548: 116501.

Johnson JS, Venturelli RA, Balco G, Allen CS, Braddock S, Campbell S, et al. (2022) Review article: Existing and potential evidence for Holocene grounding line retreat and readvance in Antarctica. *The Cryosphere* 16: 1543-1562.

Jones, V.J., Hodgson, D.A., and Chepstow-Lusty, A. (2000). Palaeolimnological evidence for marked Holocene environmental changes on Signy Island, Antarctica. *The Holocene* 10: 43-60.

Jones VJ and Juggins S. (1995) The construction of a diatom-based chlorophyll a transfer function and its application at three lakes on Signy Island (maritime Antarctic) subject to differing degrees of nutrient enrichment. *Freshwater Biology* 34: 433-445.

Juggins S. (2007) C2 Version 1.5 User Guide. Software for ecological and palaeoecological data analysis and visualisation. Newcastle University.

Juggins S. (2022) Rioja: Analysis of Quaternary Science Data, R package version (1.0-5).

Kaplan MR, Strelin JA, Schaefer JM, Denton GH, Finkel RC, Schwartz R, et al. (2011) In-situ cosmogenic ^{10}Be production rate at Lago Argentino, Patagonia: Implications for late-glacial climate chronology. *Earth and Planetary Science Letters* 309: 21-32.

Kaplan MR, Strelin JA, Schaefer JM, Peltier C, Martini MA, Flores E, et al. (2020) Holocene glacier behavior around the northern Antarctic Peninsula and possible causes. *Earth and Planetary Science Letters* 534: 116077.

Kopalová, K., & Van de Vijver, B. (2013). Structure and ecology of freshwater benthic diatom communities from Byers Peninsula, Livingston Island, South Shetland Islands. Antarctic Science, 25(2), 239-253.

Kopalová, K., Nedbalová, L., De Haan, M., and Van De Vijver, B. (2011). Description of five new species of the diatom genus Luticola (Bacillariophyta, Diadesmidaceae) found in lakes of James Ross Island (Maritime Antarctic Region). *Phytotaxa* 27: 44-60.

Kaufman D, McKay N, Routson C, Erb M, Davis B, Heiri O, et al. (2020a) A global database of Holocene paleotemperature records. *Scientific Data* 7: 115.

Kaufman, D., Mckay, N., Routson, C., Erb, M., Dätwyler, C., Sommer, P.S., Heiri, O., and Davis, B. (2020b). Holocene global mean surface temperature, a multi-method reconstruction approach. *Scientific Data* 7: 201.

Kejna M, Araźny A and Sobota I. (2013) Climatic change on King George Island in the years 1948–2011. *Polish Polar Research* 34: 213-235.

King JC and Turner J. (1997) *Antarctic Meteorology and Climatology*. Cambridge: Cambridge University Press.

Kohl CP and Nishiizumi K. (1992) Chemical isolation of quartz for measurement of in-situ -produced cosmogenic nuclides. *Geochimica et Cosmochimica Acta* 56: 3583-3587.

Lacourse T and Gajewski K. (2020) Current practices in building and reporting age-depth models. *Quaternary Research* 96: 28-38.

Lamy F, Kilian R, Arz HW, Francois J-P, Kaiser J, Prange M, et al. (2010) Holocene changes in the position and intensity of the southern westerly wind belt. *Nature Geoscience* 3: 695.

Laskar J, Robutel P, Joutel F, Gastineau M, Correia ACM and Levrard B. (2004) A long-term numerical solution for the insolation quantities of the Earth. *A&A* 428: 261-285.

Lifton N. (2016) Implications of two Holocene time-dependent geomagnetic models for cosmogenic nuclide production rate scaling. *Earth and Planetary Science Letters* 433: 257-268.

Lifton N, Sato T and Dunai TJ. (2014) Scaling in situ cosmogenic nuclide production rates using analytical approximations to atmospheric cosmic-ray fluxes. *Earth and Planetary Science Letters* 386: 149-160.

Lindow J, Castex M, Wittmann H, Johnson JS, Lisker F, Gohl K, et al. (2014) Glacial retreat in the Amundsen Sea sector, West Antarctica – first cosmogenic evidence from central Pine Island Bay and the Kohler Range. *Quaternary Science Reviews* 98: 166-173.

Liu XD, Sun LG, Xie ZQ, Yin XB and Wang YH. (2005) A 1300-year record of penguin populations at Ardley Island in the Antarctic, as deduced from the geochemical data in the ornithogenic lake sediments. *Arctic Antarctic and Alpine Research* 37: 490-498.

López-Martínez J, Serrano E, Schmid T, Mink S and Linés C. (2012) Periglacial processes and landforms in the South Shetland Islands (northern Antarctic Peninsula region). Geomorphology 155-156: 62-79.

Maclennan, J., Jull, M., Mckenzie, D., Slater, L., and Grönvold, K. (2002). The link between volcanism and deglaciation in Iceland. Geochemistry, Geophysics, Geosystems 3, 1-25.

Mann ME, Zhang Z, Rutherford S, Bradley RS, Hughes MK, Shindell D, et al. (2009) Global Signatures and Dynamical Origins of the Little Ice Age and Medieval Climate Anomaly. *Science* 326: 1256-1260.

Marcott SA, Shakun JD, Clark PU and Mix AC. (2013) A Reconstruction of Regional and Global Temperature for the Past 11,300 Years. *Science* 339: 1198-1201.

Marshall GJ. (2007) Half-century seasonal relationships between the Southern Annular mode and Antarctic temperatures. *International Journal of Climatology* 27: 373-383.

Marshall GJ, Thompson DWJ and van den Broeke MR. (2017) The Signature of Southern Hemisphere Atmospheric Circulation Patterns in Antarctic Precipitation. *Geophysical Research Letters* 44: 11,580-511,589.

Martin MA, Azorin Molina C, Utrabo Carazo E, Bedoya Valestt S and Guijarro JA. (2021) Wind speed variability over the South Shetland Islands, 1988-2019: the relationship between easterlies winds and SAM. EGU21-8706.

Masson V, Vimeux F, Jouzel J, Morgan V, Delmotte M, Ciais P, et al. (2000) Holocene Climate Variability in Antarctica Based on 11 Ice-Core Isotopic Records. *Quaternary Research* 54: 348-358.

Mäusbacher R. (1991) Die jungquartare Relief- und Klimageschichte im Bereich der Fildeshalbinsel Süd-Shetland Inseln, Antarktis. *Heidelberger Geographische Arbeiten.* Geographisches Institut der Universität Heidelberg: Heidelberg.

Mäusbacher R, Müller J and Schmidt R. (1989) Evolution of postglacial sedimentation in Antarctic lakes (King George Island). *Zeitschrift für Geomorphologie* 33: 219–234.

Meredith MP and King JC. (2005) Rapid climate change in the ocean west of the Antarctic Peninsula during the second half of the 20th century. *Geophysical Research Letters* 32: doi:10.1029/2005GL024042.

Michel RFM, Schaefer CEGR, López-Martínez J, Simas FNB, Haus NW, Serrano E, et al. (2014a) Soils and landforms from Fildes Peninsula and Ardley Island, Maritime Antarctica. *Geomorphology* 225: 76-86.

Michel RFM, Schaefer CEGR, Simas FMB, Francelino MR, Fernandes-Filho EI, Lyra GB, et al. (2014b) Active-layer thermal monitoring on the Fildes Peninsula, King George Island, maritime Antarctica. *Solid Earth* 5: 1361-1374.

Milliken KT, Anderson JB, Wellner JS, Bohaty SM and Manley PL. (2009) High-resolution Holocene climate record from Maxwell Bay, South Shetland Islands, Antarctica. *Geological Society of America Bulletin* 121: 1711-1725.

Monien P, Schnetger B, Brumsack H-J, Hass HC and Kuhn G. (2011) A geochemical record of late Holocene palaeoenvironmental changes at King George Island (maritime Antarctica). *Antarctic Science* 23: 255-267.

Moreno PI, Vilanova I, Villa-Martínez R, Dunbar RB, Mucciarone DA, Kaplan MR, et al. (2018) Onset and Evolution of Southern Annular Mode-Like Changes at Centennial Timescale. *Scientific Reports* 8: 3458.

Moreno PI, Henríquez WI, Pesce OH, Henríquez CA, Fletcher MS, Garreaud RD, et al. (2021) An early Holocene westerly minimum in the southern mid-latitudes. *Quaternary Science Reviews* 251: 106730.

Moy CM, Dunbar RB, Moreno PI, Francois J-P, Villa-Martínez R, Mucciarone DM, et al. (2008) Isotopic evidence for hydrologic change related to the westerlies in SW Patagonia, Chile, during the last millennium. *Quaternary Science Reviews* 27: 1335-1349.

Mulvaney R, Abram NJ, Hindmarsh RCA, Arrowsmith C, Fleet L, Triest J, et al. (2012) Recent Antarctic Peninsula warming relative to Holocene climate and ice-shelf history. *Nature* 489: 141-144.

Neukom R, Gergis J, Karoly DJ, Wanner H, Curran M, Elbert J, et al. (2014) Inter-hemispheric temperature variability over the past millennium. *Nature Clim. Change* 4: 362-367.

Nývlt D, Glasser NF, Hocking E, Oliva M, Roberts SJ and Roman M. (2020) Chapter 5 - Tracing the deglaciation since the Last Glacial Maximum. In: Oliva M and Ruiz-Fernández J (eds) Past Antarctica. Academic Press, 89-107.

Ó Cofaigh C, Davies BJ, Livingstone SJ, Smith JA, Johnson JS, Hocking EP, et al. (2014) Reconstruction of ice-sheet changes in the Antarctic Peninsula since the Last Glacial Maximum. *Quaternary Science Reviews* 100: 87-110.

Oksanen J. (2014) Vegan: Community Ecology Package. R package version 2.3-0. http://cran.r-project.org/web/packages/vegan/index.html.

Oliva M, Navarro F, Hrbáček F, Hernández A, Nývlt D, Pereira P, et al. (2017) Recent regional climate cooling on the Antarctic Peninsula and associated impacts on the cryosphere. *Science of The Total Environment* 580: 210-223.

Oliva M, Antoniades D, Serrano E, Giralt S, Liu EJ, Granados I, et al. (2019) The deglaciation of Barton Peninsula (King George Island, South Shetland Islands, Antarctica) based on geomorphological evidence and lacustrine records. *Polar Record* 55: 177-188.

Oliva M, Mercier D, Ruiz-Fernández J and McColl S. (2020) Paraglacial processes in recently deglaciated environments. *Land Degradation & Development* 31: 1871-1876.

Palacios D, Ruiz-Fernández J, Oliva M, Andrés N, Fernández-Fernández JM, Schimmelpfennig I, et al. (2020) Timing of formation of neoglacial landforms in the South Shetland Islands (Antarctic Peninsula): Regional and global implications. *Quaternary Science Reviews* 234: 106248.

Pallàs R, James T, Sàbat F, Vilaplana J, Grant D and Ricci C. (1997) Holocene uplift in the South Shetland Islands: evaluation of tectonics and glacio-isostasy. In: Ricci C (ed) The Antarctic Region: Geological Evolution and Processes. Siena, Italy: Terra Antarctica Publication, 861–868.

Parnell AC. (2021) Bchron: Radiocarbon Dating, Age-Depth Modelling, Relative Sea Level Rate Estimation, and Non-Parametric Phase Modelling. *https://github.com/andrewcparnell/Bchron/*.

Perren BB, Hodgson DA, Roberts SJ, Sime L, Van Nieuwenhuyze W, Verleyen E, et al. (2020) Southward migration of the Southern Hemisphere westerly winds corresponds with warming climate over centennial timescales. *Communications Earth & Environment* 1: 58.

Praetorius, S., Mix, A., Jensen, B., Froese, D., Milne, G., Wolhowe, M., Addison, J., and Prahl, F. (2016). Interaction between climate, volcanism, and isostatic rebound in Southeast Alaska during the last deglaciation. Earth and Planetary Science Letters 452, 79-89.

Putnam AE, Schaefer JM, Barrell DJA, Vandergoes M, Denton GH, Kaplan MR, et al. (2010) In situ cosmogenic 10Be production-rate calibration from the Southern Alps, New Zealand. *Quaternary Geochronology* 5: 392-409.

Quade J and Kaplan MR. (2017) Lake-level stratigraphy and geochronology revisited at Lago (Lake) Cardiel, Argentina, and changes in the Southern Hemispheric Westerlies over the last 25 ka. *Quaternary Science Reviews* 177: 173-188.

Reimer RW, and Reimer PJ. (2004). CALIBomb - calibration of post-bomb C-14 data (www.calib.org).

Reynhout SA, Sagredo EA, Kaplan MR, Aravena JC, Martini MA, Moreno PI, et al. (2019) Holocene glacier fluctuations in Patagonia are modulated by summer insolation intensity and paced by Southern Annular Mode-like variability. *Quaternary Science Reviews* 220: 178-187.

Roberts SJ, Hodgson DA, Bentley MJ, Smith JA, Millar IL, Olive V, et al. (2008) The Holocene history of George VI Ice Shelf, Antarctic Peninsula from clast-provenance analysis of epishelf lake sediments. *Palaeogeography Palaeoclimatology Palaeoecology* 259: 258-283.

Roberts SJ, Hodgson DA, Shelley S, Royles J, Griffiths HJ, Deen TJ, et al. (2010) Establishing Lichenometric Ages for Nineteenth- and Twentieth-Century Glacier Fluctuations on South Georgia (South Atlantic). *Geografiska Annaler Series a-Physical Geography* 92A: 125-139.

Roberts SJ, Hodgson DA, Sterken M, Whitehouse PL, Verleyen E, Vyverman W, et al. (2011) Geological constraints on glacio-isostatic adjustment models of relative sea-level change during deglaciation of Prince Gustav Channel, Antarctic Peninsula. *Quaternary Science Reviews* 30: 3603-3617.

Roberts SJ, Monien P, Foster LC, Loftfield J, Hocking EP, Schnetger B, et al. (2017) Past penguin colony responses to explosive volcanism on the Antarctic Peninsula. *Nature Communications* 8: 14914.

Roberts SJ, McCulloch RD, Emmings JF, Davies SJ, Van Nieuwenhuyze W, Sterken M, et al. (2022) Late Glacial and Holocene Palaeolake History of the Última Esperanza Region of Southern Patagonia. *Frontiers in Earth Science* 10. doi:10.3389/feart.2022.813396

Satow C, Gudmundsson A, Gertisser R, Ramsey CB, Bazargan M, Pyle DM, et al. (2021) Eruptive activity of the Santorini Volcano controlled by sea-level rise and fall. *Nature Geoscience* 14: 586-592.

Saunders KM, Roberts SJ, Perren B, Butz C, Sime L, Davies S, et al. (2018) Holocene dynamics of the Southern Hemisphere westerly winds and possible links to CO2 outgassing. *Nature Geoscience* 11: 650-655.

Schmidt R, Mäusbacher R and Müller J. (1990) Holocene diatom flora and stratigraphy from sediment cores of two Antarctic lakes (King George Island). *Journal of Paleolimnology* 3: 55-74.

Seong YB, Owen LA, Lim HS, Yoon HI, Kim Y, Lee YI, et al. (2008) Rate of late Quaternary ice-cap thinning on King George Island, South Shetland Islands, West Antarctica defined by cosmogenic 36Cl surface exposure dating. *Boreas* 38: 207-213.

Simms AR, Milliken KT, Anderson JB and Wellner JS. (2011) The marine record of deglaciation of the South Shetland Islands, Antarctica since the Last Glacial Maximum. *Quaternary Science Reviews* 30: 1583-1601.

Simms AR, Ivins ER, DeWitt R, Kouremenos P and Simkins LM. (2012) Timing of the most recent Neoglacial advance and retreat in the South Shetland Islands, Antarctic Peninsula: insights from raised beaches and Holocene uplift rates. *Quaternary Science Reviews* 47: 41-55.

Simms AR, Whitehouse PL, Simkins LM, Nield G, DeWitt R and Bentley MJ. (2018) Late Holocene relative sea levels near Palmer Station, northern Antarctic Peninsula, strongly controlled by late Holocene ice-mass changes. *Quaternary Science Reviews* 199: 49-59.

Simms AR, Lisiecki L, Gebbie G, Whitehouse PL and Clark JF. (2019) Balancing the last glacial maximum (LGM) sea-level budget. *Quaternary Science Reviews* 205: 143-153.

Simms AR, Bentley MJ, Simkins LM, Zurbuchen J, Reynolds LC, DeWitt R, et al. (2021) Evidence for a “Little Ice Age” glacial advance within the Antarctic Peninsula – Examples from glacially-overrun raised beaches. *Quaternary Science Reviews* 271: 107195.

Smellie JL, Pankhurst R, Thomson MRA and Davies RES. (1984) The geology of the South Shetland Islands: VI. Stratigraphy, geochemistry and evolution. *British Antarctic Survey Scientific Reports* 87: 85 pp.

Steinhilber F, Beer J and Fröhlich C. (2009) Total solar irradiance during the Holocene. *Geophysical Research Letters* 36: L19704.

Sterken, M., Roberts, S., Hodgson, D., Vyverman, W., Balbo, A.L., Sabbe, K., Moreton, S.G., and Verleyen, E. (2012). Holocene glacial and climate history of Prince Gustav Channel, northeastern Antarctic Peninsula. *Quaternary Science Reviews* 31: 93-111.

Sterken, M., Verleyen, E., Jones, V.J., Hodgson, D.A., Vyverman, W., Sabbe, K., and Van De Vijver, B. (2015). An illustrated and annotated checklist of freshwater diatoms (Bacillariophyta) from Livingston, Signy and Beak Island (Maritime Antarctic Region). *Plant Ecology and Evolution* 148: 431-455.

Strelin JA, Kaplan MR, Vandergoes MJ, Denton GH and Schaefer JM. (2014) Holocene glacier history of the Lago Argentino basin, Southern Patagonian Icefield. *Quaternary Science Reviews* 101: 124-145.

Stone, J.O. (2000). Air pressure and cosmogenic isotope production. *Journal of Geophysical Research: Solid Earth* 105: 23753-23759.

Sugden DE and Clapperton CM. (1977) The maximum ice extent on island groups in the Scotia sea, Antarctica. *Quaternary Research* 7: 268-282.

Sugden DE and John BS. (1973) The ages of glacier fluctuations in the South Shetland Islands, Antarctica. In: van Zinderen; Bakker EM (ed) *Palaeoecology of Africa, the Surrounding Islands and Antarctica.* Balkema, Cape Town, 141-159.

Sun LG, Liu XD, Yin XB, Xie ZQ and Zhao JL. (2005) Sediments in palaeo-notches: potential proxy records for palaeoclimatic changes in Antarctica. *Palaeogeography, Palaeoclimatology, Palaeoecology* 218: 175-193.

Tatur A, Martinez-Macchiavello JC, Niegodzisz J and del Valle R. (1999) A record of Holocene environmental changes in sediment core of Hotel Lake, King George Island, Antarctica. *Polish Polar Studies* 26 Polar Symposium.

Thomas ER, Marshall GJ and McConnell JR. (2008) A doubling in snow accumulation in the western Antarctic Peninsula since 1850. *Geophysical Research Letters* 35: L01706.

Turner J, Lachlan-Cope TA, Marshall GJ, et al. (2002) Spatial variability of Antarctic Peninsula net surface mass balance. *Journal of Geophysical Research: Atmospheres* 107: AAC 4-1-AAC 4-18.

Turner J, Colwell SR, Marshall GJ, Lachlan-Cope TA, Carleton AM, Jones PD, et al. (2004) The SCAR READER Project: Toward a High-Quality Database of Mean Antarctic Meteorological Observations. *Journal of Climate* 17: 2890-2898.

Turner J, Lu H, White I, King JC, Phillips T, Hosking JS, et al. (2016) Absence of 21st century warming on Antarctic Peninsula consistent with natural variability. *Nature* 535: 411-415.

van der Bilt WGM, Bakke J, Werner JP, Paasche Ø, Rosqvist G and Vatle SS. (2017) Late Holocene glacier reconstruction reveals retreat behind present limits and two-stage Little Ice Age on subantarctic South Georgia. *Journal of Quaternary Science* 32: 888-901.

van der Wal W, Whitehouse PL and Schrama EJO. (2015) Effect of GIA models with 3D composite mantle viscosity on GRACE mass balance estimates for Antarctica. *Earth and Planetary Science Letters* 414: 134-143.

Varma V, Prange M, Merkel U, Kleinen T, Lohmann G, Pfeiffer M, et al. (2012) Holocene evolution of the Southern Hemisphere westerly winds in transient simulations with global climate models. *Climate of the Past* 8: 391-402.

Vaughan DG, Marshall G, Connolley WM, Parkinson C, Mulvaney R, Hodgson DA, et al. (2003) Recent rapid regional climate warming on the Antarctic Peninsula. *Climatic Change* 60: 243-274.

Verfaillie D, Charton J, Schimmelpfennig I, Stroebele Z, Jomelli V, Bétard F, et al. (2021) Evolution of the Cook Ice Cap (Kerguelen Islands) between the last centuries and 2100 ce based on cosmogenic dating and glacio-climatic modelling. *Antarctic Science* 33: 301-317.

Verleyen E, Tavernier I, Hodgson DA, Whitehouse PL, Kudoh S, Imura S, et al. (2017) Ice sheet retreat and glacio-isostatic adjustment in Lützow-Holm Bay, East Antarctica. *Quaternary Science Reviews* 169: 85-98.

Wang G and Cai W. (2013) Climate-change impact on the 20th-century relationship between the Southern Annular Mode and global mean temperature. *Scientific Reports* 3: 2039.

Watcham EP, Bentley MJ, Hodgson DA, Roberts SJ, Fretwell PT, Lloyd JM, et al. (2011) A new Holocene relative sea level curve for the South Shetland Islands, Antarctica. *Quaternary Science Reviews* 30: 3152-3170.

Weatherall P, Marks KM, Jakobsson M, Schmitt T, Tani S, Arndt JE, et al. (2015) A new digital bathymetric model of the world's oceans. *Earth and Space Science* 2: 331-345.

Whitehouse PL, Bentley MJ and Le Brocq AM. (2012a) A deglacial model for Antarctica: geological constraints and glaciological modelling as a basis for a new model of Antarctic glacial isostatic adjustment. *Quaternary Science Reviews* 32: 1-24.

Whitehouse PL, Bentley MJ, Milne GA, King MA and Thomas ID. (2012b) A new glacial isostatic adjustment model for Antarctica: calibrated and tested using observations of relative sea-level change and present-day uplift rates. *Geophysical Journal International* 190: 1464-1482.

Yang L, Gao Y, Sun L, Xie Z, Yang W, Chu Z, et al. (2019) Enhanced westerlies drove penguin movement at 1000 yr BP on Ardley Island, west Antarctic Peninsula. *Quaternary Science Reviews* 214: 44-53.

Yoon H-I, Khim B-K, Lee K, Park Y-H and Yoo K-C. (2006) Reconstruction of postglacial paleoproductivity in Long Lake, King George Island, West Antarctica. *Polish Polar Research* 7: 189-206.

Yu Z, Beilman DW and Loisel J. (2016) Transformations of landscape and peat-forming ecosystems in response to late Holocene climate change in the western Antarctic Peninsula. *Geophysical Research Letters* 43: 7186-7195.

Zurbuchen J and Simms AR. (2019) Late Holocene ice-mass changes recorded in a relative sea-level record from Joinville Island, Antarctica. *Geology* 47: 1064-1068.